Università degli Studi di Napoli Federico II

Scuola Politecnica e delle Scienze di Base
Dipartimento di Fisica "Ettore Pancini"

Corso di Laurea in Fisica

Anno Accademico 2018/2019

Tesi di Laurea Magistrale

Dissipation in superconducting NbN and NbTiN nanostructures

Relatore:
Prof. Francesco Tafuri
Dr. Davide Massarotti

Candidato:
Luca Cozzolino
Matricola: N94/427

Contents

Introduction

Superconducting nanostructures allow to investigate frontier problems in solid state physics and favor a large number of applications, which touch other field of reserach activity. Nanowires for instance have been of increasing interest in the last years, due to their possible use as superconducting nanowire single photon detectors (SNSPD) in quantum technologies. These devices show an intrinsic transistion from the superconducting to the resistive state when a certain current I_{sw} flows through the sample. The detection principle is based on this transition: as the photon impacts the active region of the SNSPD, it warms up the nanowire, causing the transition to the normal state and thus a voltage drop that can be measured. To characterise the dark counts rate of these detectors, it is fundamental to study the dissipation processes in these superconducting nanostructures.
To completely characterise the nanostructures behaviours at different temperatures, it is necessary to study the dissipation modes and self-heating process, which are the main target of this thesis and are specifically relevant to determine the dark count rates of these photon detectors. For this reason, I-V characteristics and switching current distributions (SCDs) of the nanostructures have been measured in a range of temperatures from few mK to temperatures relatively close to the critical temperature T_c.
After a brief introduction to superconductivity and its principal theories in Chapter 1, one of the main models to describe superconducting to resistive state transistion, the thermally activated phase slips (TAPS) model, is presented. The switching transistions are strongly correlated with the self-heating process, as it will be clear at the end of the chapter.
Once the self-heating process has been presented, in Chapter 2, it is widely discussed the connection between the I-V characteristics and the SCDs, which are the principal experimental investigation tools to explore the heating dynamics. Indeed, the description of the SCDs is discussed in terms of the local heat dynamics, presented in Section 2.3.
In order to give an overview on the experimental background, in Chapter 3 the cryogenic systems used to collect the measurements are described. Then, the measurement setup and protocols are described, with a final discussion about the

measurement errors.
Finally, the experimental data are discussed in Chapter 4 and compared with theoretical curves obtained by the local heat dynamics model. The fitting curves and parameters allow an insight on the dissipation processes in the different nanostructures.
It is shown that the behaviour of these nanodevices is completely described by the local heat dynamics in the whole temperature range used in the measurements. The presence of two possible processes at the origin of the switching transistion, which are identified in the single and the multiple phase slip regime, is presented to describe these behaviours.

Chapter 1

Superconductivity in nanostructures

Superconductivity is a physical phenomenon discovered in the early years of XX century and it has been observed in more the 30 elements, and in a larger number of alloys [1], below a certain transition temperature called critical temperature T_c characteristic of each specific material. A superconductor can be identified by two hallmarks:

- perfect conductivity [2];
- perfect diamagnetism [3, 4].

It will be first briefly mentioned the microscopic theory by Bardeen-Cooper-Schrieffer (BCS), which explains the origin of superconductivity, and the phenomenological Ginzburg-Landau (GL) theory in order to introduce some important physical parameters used in this work. It is possible to derive the GL theory from the BCS one, so that the predictions are consistent [5].
Then, the *phase slips* concept and model will be presented as a possible origin of the superconducting to resistive state transition in superconducting nanostructures.
These notions will provide the background to discuss the mechanisms leading to dissipation in nanostructured superconductors, which is the ultimate aim of this work.

1.1 Principal phenomena

In 1911, by performing measurements of the resistance of mercury, Kamerlingh Onnes found a vanishing resistance below a critical temperature of $T_c = 4.2\,\mathrm{K}$

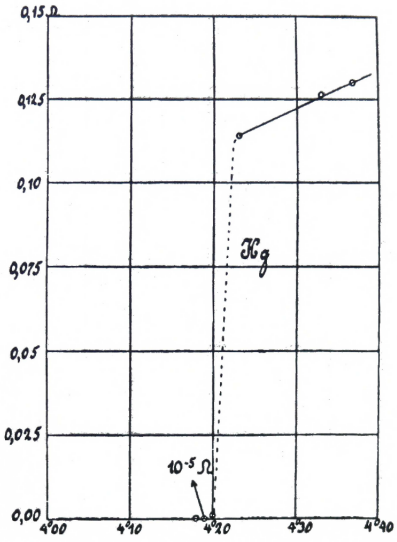

Figure 1.1: First observation of resistance drop in Hg [2].

[2]. A modern and more accurate demonstration of perfect conduction is realised through an expriment using a superconducting ring. Typically, current in a ring varies in time according to

$$I(t) = I(0)e^{-\frac{R(T)t}{L}}$$

where $R(T)$ is the resistance and L the inductance of the ring respectively. In experiments with superconductors no significant variation of the current has been measured [6].
In 1933, Meissner and Ochsenfeld discovered the perfect diamagnetism of superconductors in a magnetic field [3]. However, such an effect cannot be explained by only considering a superconductor as a perfect conductor. Indeed, in Figure 1.2, the differences between the behaviours of a perfect conductor and a superconductor in a magnetic field are presented.

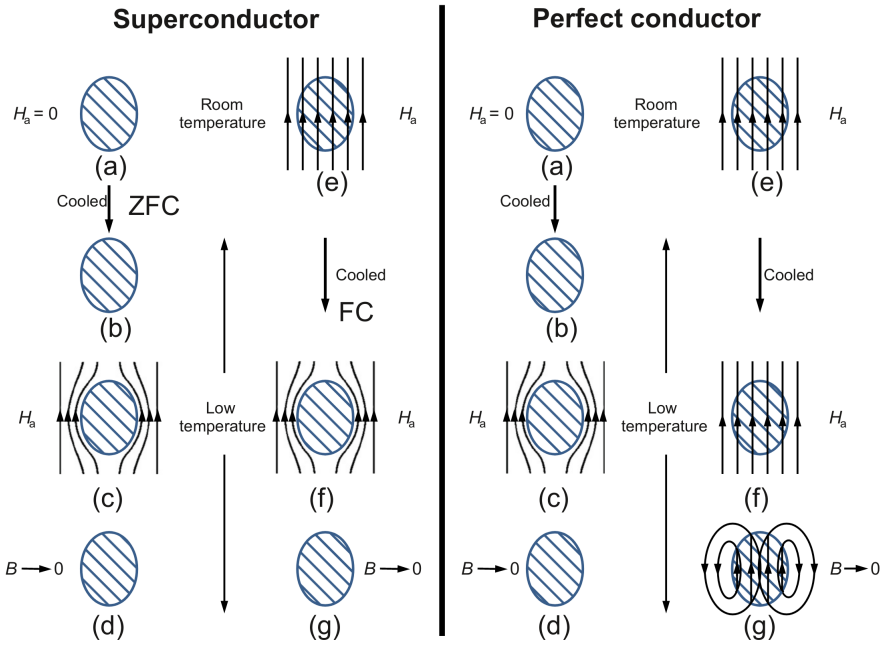

Figure 1.2: Differences between superconductor and a perfect conductor [7].

A first theory capable of explaining the relation between the perfect conductivity and the perfect diamagnetism was presented by F. and H. London in 1935 [4]: they proposed two equations on microscopic magnetic and electric fields, which lead to an exponetial screening of magnetic field within a length given by the penetration depth λ_L

$$\lambda_L^2(0) = \frac{mc^2}{4\pi n_s e^2} \tag{1.1}$$

here presented in the limit of $T = 0$, where the density of superconducting electrons n_s is the same of the conduction electron one. London equations are still a phenomenological theory but, in 1950, F. London proposed to describe superconductivity as a quantum phenomenon on a macroscopic scale [8]. In this view, n_s can be written as the *superfluid density* $|\psi|^2$, as if the superconducting electrons where in something like a Bose-Einstein condensed phase.

1.2 Bardeen-Cooper-Schrieffer theory

In 1956, Corak *et al.* experimentally showed that the electronic specific heat in superconducting vanadium has an exponential trend [9]:

$$C_{es} \approx \gamma a T_c e^{-\frac{bT}{T_c}}$$

instead of the linear behaviour of the electronic specific heat typical of the normal state $C_{en} = \gamma T$, where a and b are numerical constants ($b \approx 1.5$) and γ is a constant that can be determined experimentally [9]. This and other measurements would be explainable if the excitations were produced in pair, and not by single indipendent particles [10]. In this framework, Bardeen, Cooper and Schrieffer proposed a theory where superconductivity is due to an interaction mediated by phonons between electron pairs, the so-called *Cooper pairs*. Indeed, an electron passing through the lattice polarizes the nearby ions. Before lattice relaxation, another electron is attracted by positive polarized ions [11]. Thus, the two electrons form a Cooper pair, which behave like a single boson and is characterised by a superconducting coherence length $\xi(T)$, i.e the maximum length needed to form the pair. The maximum of attraction occurs when the two electrons have an opposite momentum $\boldsymbol{k}$. This pairing condition, in addition to a contact-potential interaction in real space, leads to the following Hamiltonian of an electronic system in a bulk superconductor in Hartree-Fock approximation, written in second quantization formalism [10]:

$$\mathscr{H} = \sum_{\boldsymbol{k}\sigma} \epsilon_{\boldsymbol{k}} c^{\dagger}_{\boldsymbol{k}\sigma} c_{\boldsymbol{k}\sigma} + \sum_{\boldsymbol{k},\boldsymbol{l}} V_{\boldsymbol{k},\boldsymbol{l}} c^{\dagger}_{\boldsymbol{k}\uparrow} c^{\dagger}_{-\boldsymbol{k}\downarrow} c_{-\boldsymbol{l}\downarrow} c_{\boldsymbol{l}\uparrow} \tag{1.2}$$

where $\epsilon_{\boldsymbol{k}} = \dfrac{\hbar^2 k^2}{2m} - E_F$ and

$$V_{\boldsymbol{k},\boldsymbol{l}} = \begin{cases} -V & \text{for } |\epsilon_{\boldsymbol{l}}|, |\epsilon_{\boldsymbol{k}}| \leq \hbar\omega_D \\ 0 & \text{otherwise} \end{cases} \tag{1.3}$$

where E_F is the Fermi energy, ω_D the Debye frequency and V a positive constant. To find the ground state of Equation (1.2), the following trial wavefunction is used in a variational method

$$|\Psi\rangle = \prod_{\boldsymbol{k}} \left(u_{\boldsymbol{k}} + v_{\boldsymbol{k}} c^{\dagger}_{\boldsymbol{k},\uparrow} c^{\dagger}_{-\boldsymbol{k},\downarrow} \right) |0\rangle \tag{1.4}$$

with the normalisation condition

$$|u_{\boldsymbol{k}}|^2 + |v_{\boldsymbol{k}}|^2 = 1 \quad .$$

From these equations, the amplitude of Cooper pairs is

$$u_{\boldsymbol{k}} v_{\boldsymbol{k}} = \frac{1}{2} \frac{\Delta_{\boldsymbol{k}}}{E_{\boldsymbol{k}}}$$

where $E_{\boldsymbol{k}} = \sqrt{\epsilon^2_{\boldsymbol{k}} + \Delta^2_{\boldsymbol{k}}}$ is the quasi-particle excitation spectrum [10]. Indeed, whereas the Cooper pairs condense in a ground state, the excitations can be seen as

quasi-particle, also known as *bogoliubons*[1], that are a superposition of electrons and holes. As it can be noted from the energy-momentum diagram (Figure 1.3a), in a normal metal the electron-hole pair creation is seen like the excitation of two states: a hole of energy E_h, below the Fermi level, and an electron of energy E_l, above the Fermi level. In the same way, in Figure 1.3b, in a superconducting metal, all the Cooper pairs are at the Fermi level and an excitation needs a minimum threshold energy, that is the superconducting gap Δ. Thus, an excitation is partially in a hole and partially in an electron state [12].

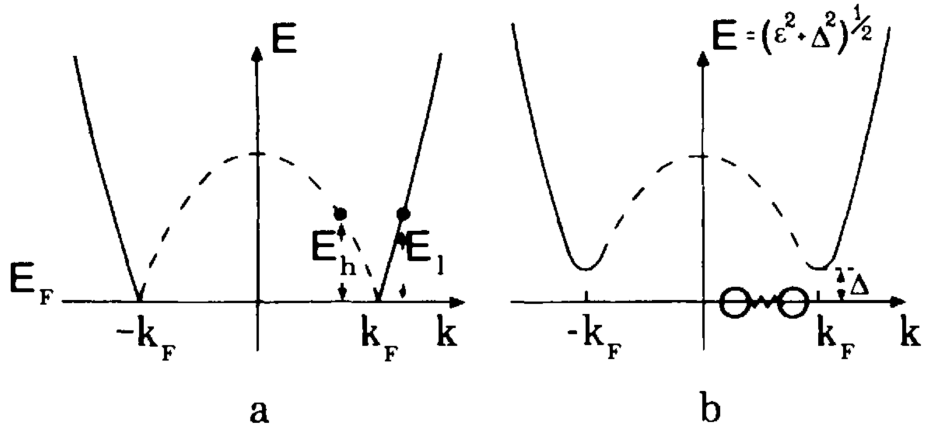

Figure 1.3: Energy momentum diagrams: the dashed line rappresents the energy levels below the Fermi level. In panel (a) there is the electron-hole pair creation in a normal metal. In panel (b) Cooper pairs in a superconductor [12].

Since there is a one-to-one corrispondence between quasi-particle excitations and electrons in the normal state, the density of states (DOS) can be derived by considering the following relation:

$$D(E)dE = \mathscr{D}(\epsilon)d\epsilon$$

where $\mathscr{D}(\epsilon)$ is the normal state DOS and $D(E)$ is the superconducting one. Thus,

$$\frac{D(E)}{\mathscr{D}(\epsilon)} = \frac{d\epsilon}{dE} = \frac{E}{\sqrt{E^2 - \Delta^2(E)}} - \frac{\Delta(E)[d\Delta(E)/dE]}{\sqrt{E^2 - \Delta^2(E)}} \quad . \tag{1.5}$$

In case of an energy indipendent gap [12], Equation (1.5) can be written as

$$D(E) = \mathscr{D}(\epsilon)\frac{E}{\sqrt{E^2 - \Delta^2}}$$

where the superconducting gap Δ is ralated to T_c [13]

$$\Delta = 1.76 k_B T_c \quad . \tag{1.6}$$

[1]This name derives from the Bogoliubov-Valatin tranformation applied to Equation (1.2).

1.3 Ginzburg-Landau theory

The GL theory is a phenomenological theory [14], formulated before the BCS theory. In 1959 Gork'ov showed that the GL equations could be derived from the microscopic theory, rewritten in terms of Green functions in order to treat inhomogenity [5].
Since the superconductor-normal transition is a second-order phase transition [2], Ginzburg and Landau formulated a mean field theory valid below T_c, using a complex order parameter ψ:

$$\psi = \sqrt{\frac{n_s}{2}} e^{\imath\varphi} \tag{1.7}$$

where φ is the phase and $|\psi|^2 = n_s/2 = \rho_s$ is the density of *superelectrons*. Within the framework of the GL theory, it is possible to rewrite the free-energy as a functional of the order parameter ψ, expanding the free-energy density in terms of the order parameter and its derivatives [15]:

$$F = F_{n_0} + \int \left\{ \frac{\boldsymbol{B}^2}{8\pi} + \frac{\hbar^2}{4m} \left| \left(\nabla - \frac{2\imath e}{\hbar c} \boldsymbol{A} \right) \psi \right|^2 + a|\psi|^2 + \frac{b}{2}|\psi|^4 \right\} dV \tag{1.8}$$

where F_{n_0} is the free-energy of the normal state and the expansion coefficients $a = A(T - T_c)$ and b are positive. The spatial distribution of ψ and the magnetic field in the superconductor is given by the minimum of Equation (1.8), that is a functional of ψ, ψ^* and $\boldsymbol{A}$. By varying ψ^* in Equation (1.8), the minimum of δF for any $\delta\psi^*$ is

$$\frac{\delta F}{\delta \psi *} = \frac{1}{4m} \left(-\imath\hbar\nabla - \frac{2e}{c}\boldsymbol{A} \right)^2 \psi + a\psi + b|\psi|^2\psi = 0 \tag{1.9}$$

In the same way, the variation of $\boldsymbol{A}$ brings to

$$\boldsymbol{\nabla} \times \boldsymbol{B} = \frac{4\pi}{c}\boldsymbol{j} \tag{1.10}$$

where the current density is given by

$$\boldsymbol{j} = -\frac{\imath e\hbar}{2m}(\psi^*\boldsymbol{\nabla}\psi - \psi\boldsymbol{\nabla}\psi^*) - \frac{2e^2}{mc}|\psi|^2\boldsymbol{A} \tag{1.11}$$

[2] Second-order phase transitions are characterised by continuous first derivative of the free-energy with respect to some thermodynamic variable and show a discontinuity in the second derivative.

Equations (1.9) and (1.11) are the so-called *Ginzburg-Landau equations*, that have been used by Langer and Ambegaokar [16] for the phase slip process in superconducting nanostructures, which will be analysed in Section 1.6. In these equations the coherence length of order parameter can be found:

$$\xi(T) = \frac{\hbar}{2(mA)^{1/2}\sqrt{Tc - T}} \tag{1.12}$$

Moreover, from Equations (1.10) and (1.11), the London equations can be found and thus the penetration depth:

$$\lambda(T) = \sqrt{\frac{mc^2 b}{8\pi e^2 A(T_c - T)}} \quad . \tag{1.13}$$

These two quantities (coherence length and penetration depth) are fundamental in the definition of the Ginzburg-Landau parameter κ:

$$\kappa = \frac{\lambda(T)}{\xi(T)} = \frac{mcb^{1/2}}{\sqrt{2\pi}|e|\hbar} \quad . \tag{1.14}$$

The GL parameter allows to distinguish between two kinds of superconductors:

$$\begin{cases} \text{Type I} & \text{for } 0 < \kappa < 1/\sqrt{2} \\ \text{Type II} & \text{for } \kappa > 1/\sqrt{2} \end{cases} \tag{1.15}$$

These two superconductors classes have extremely different behaviours as can be seen from their response to an external magnetic field.

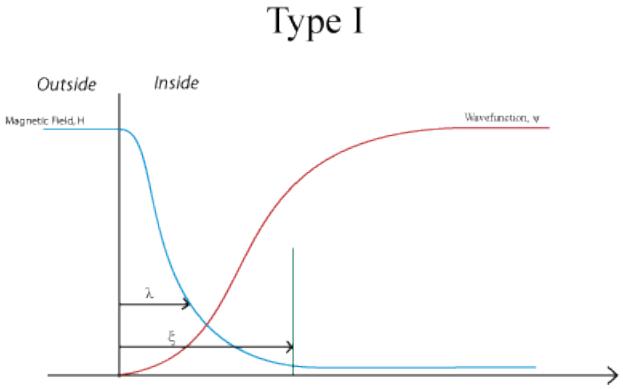

Figure 1.4: Applied field and order parameter behaviours inside and outside a bulk Type I superconductor [17].

Indeed, looking at what happens at the boundary of a Type I superconductor, as depicted in Figure 1.4, a magnetic field penetrates in a small region, exponentially decaying, and it is expelled from the bulk, until a critical field H_c is reached. This field can destroy the superconducting state and is related to the difference between the Helmholtz free-energies of superconducting and normal phases:

$$E_c = \frac{H_c^2(T)}{8\pi} = f_s(T) - f_n(T) \tag{1.16}$$

where E_c is the so-called condensation energy [10].
On the other hand, Type II superconductors are characterised by a continuous increase of flux penetration.

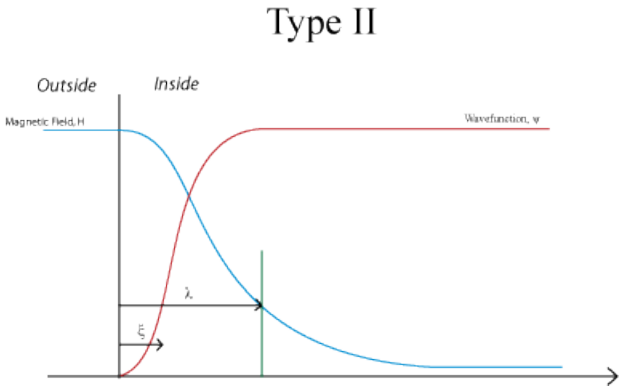

Figure 1.5: Applied field and order parameter behaviours inside and outside a bulk Type II superconductor [17].

Indeed, as the magnetic field reaches a "first" critical field H_{c_1}, magnetic flux penetrates in the superconductor, until H reaches a "second" critical field H_{c_2}, where the superconductivity is lost.

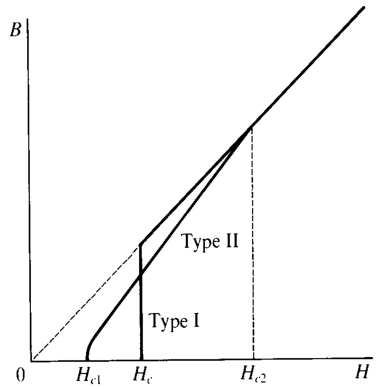

Figure 1.6: The internal field B with the respect to an applied external field H for a Type I and a Type II superconductor with the same thermodynamic critical field H_c [10]

Abrikosov, that firstly described Type II superconductors [18], noticed that between H_{c_1} and H_{c_2}, the material is in the so-called *mixed state* or *Schubnikov phase*, where the flux penetrates in regular array of flux tubes, each one carring a flux quantum $\Phi_0 = h/2e$. In every cell of the array, the flux is generated by a supercurrent vortex toward the center of the vortex itself [10].

1.3.1 Time-dependent GL theory

To study the relaxation of the system when it is not in an equilibrium state, it is needed a time-dependent GL theory. As reported in Ref. [19, 20], the simplest equation for ψ is given by:

$$\gamma\hbar\frac{\partial\psi}{\partial t} = \frac{1}{2m}(\hbar\nabla)^2\psi + a(T)\psi + b|\psi|^2\psi \tag{1.17}$$

from which it can be seen that there is a time constant τ_{GL}, called Ginzburg-Landau relaxation time [11], correlated to T and T_c

$$\tau_{GL} = \frac{\hbar\gamma}{2a} = \frac{\pi\hbar}{8k_B(T-T_c)} \quad . \tag{1.18}$$

In presence of an external field, Equation (1.17) has to be modified to take into account the magnetic field:

$$\left(\imath\hbar\frac{\partial}{\partial t} - 2\mu\right)\psi = -\frac{\imath}{\tau_{GL}}\frac{\hbar}{|a(T)|}\frac{\partial F}{\partial\psi^*} \tag{1.19}$$

where μ is the chemical potential and $\partial F/\partial\psi^*$ has been defined in Equation (1.9). Although the form presented in Equation (1.19) of a time-dependent GL theory

should be accurate only near T_c [19], McCumber and Halperin have used it for their model (that will be described in Section 1.6.1), which is in agreement with the experiments even well below T_c.

1.4 Josephson effect

One of the most interesting effects regarding superconductors was predicted by Josephson in 1962 [21]. As it is presented below in this section, the most impressive effect of the Josephson effect is the *supercurrent* flow through a small barrier between two superconductors without a voltage drop, which has been experimentally observed in 1963 [22] for the first time. Considering two superconductors coupled by a weak link (Figure 1.7), such as an insulating barrier, Cooper pairs flow from a superconductor to another without a voltage drop, until a maximum value of the supercurrent is reached. Josephson found out that the current flow through the barrier is deeply correlated with the phase difference between the two superconductors that constitute the Josephson junction. For this reason, Josephson junctions are the main benchmark for the study of the phase dynamics in superconducting nanodevices.
If we take into account the two order parameters ψ_R and ψ_L for the right and left superconductor respectively, it has been shown that

$$\langle R|\, \psi_R^* \psi_R \,|R\rangle = |\psi_R|^2 = \rho_R \qquad\qquad \langle L|\, \psi_L^* \psi_L \,|L\rangle = |\psi_L|^2 = \rho_L \tag{1.20}$$

where $|R\rangle$ and $|L\rangle$ are the macroscopic states of the right and left superconductor respectively [12].

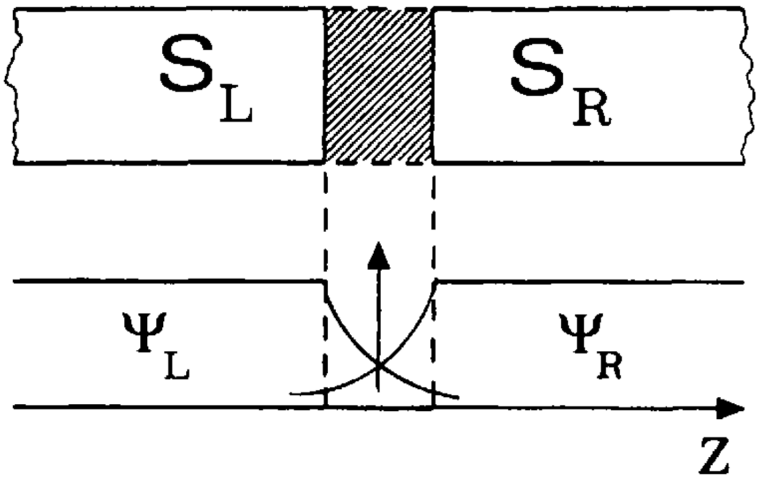

Figure 1.7: Order parameters overlap in the insulating barrier between S_R and S_L superconductors [12].

This coupling is due to the overlap of ψ_R and ψ_L, as depicted in Figure 1.7, and the whole system can be described by

$$|\psi\rangle = \psi_R |R\rangle + \psi_L |L\rangle \quad . \tag{1.21}$$

The macrostate $|\psi\rangle$ has a time evolution given by the Schrödinger equation where the hamiltonian is

$$\mathscr{H} = \mathscr{H}_L + \mathscr{H}_R + \mathscr{H}_T = E_L |L\rangle \langle L| + E_R |R\rangle \langle R| + K[|L\rangle \langle R| + |R\rangle \langle L|] . \tag{1.22}$$

The first two terms in Equation (1.22) are the imperturbated hamiltonians of the righ and left superconductor and $\mathscr{H}_T$ is the tunneling hamiltonian. $E_R = 2\mu_R$ and $E_L = 2\mu_L$ are the ground state energies of the two superconductors, whereas K is the coupling amplitude and it depends essentially on the junction structure.
The Scrödinger equation can be projected on the base states, leading to the time evolution equation of ψ_R and ψ_L

$$\imath\hbar\frac{\partial\psi_L}{\partial t} = E_L\psi_L + K\psi_R \tag{1.23}$$

$$\imath\hbar\frac{\partial\psi_R}{\partial t} = E_R\psi_R + K\psi_L \quad . \tag{1.24}$$

If there is a potential difference V between the two superconductors, the chemical potentials are shifted by eV, so that $E_L - E_R = 2eV$: thus it is possible to set the zero of energy such that $E_R = -eV$ and $E_L = eV$.
Recalling Equation (1.7), it can be found a set of equations describing supercurrent

flow and the time evolution of the phase difference of the two electrodes of the Josephson junction [12]. Thus, it is possible to define a pair current density through the barrier as

$$J \equiv \frac{\partial \rho_L}{\partial t} = -\frac{\partial \rho_R}{\partial t} = \frac{2K}{\hbar}\sqrt{\rho_L \rho_R}\sin\varphi = J_1 \sin\varphi \tag{1.25}$$

where J_1 is the maximum supercurrent density and $\varphi = \varphi_L - \varphi_R$ is the phase difference between the two electrodes.
The time evolution of the phase difference φ can be found as [12, 21]:

$$\frac{\partial \varphi}{\partial t} = \frac{2eV}{\hbar} \quad . \tag{1.26}$$

Equations (1.25) and (1.26) are the so-called *Josephson equations*. A typical *I-V* characteristic is reported in the following figure.

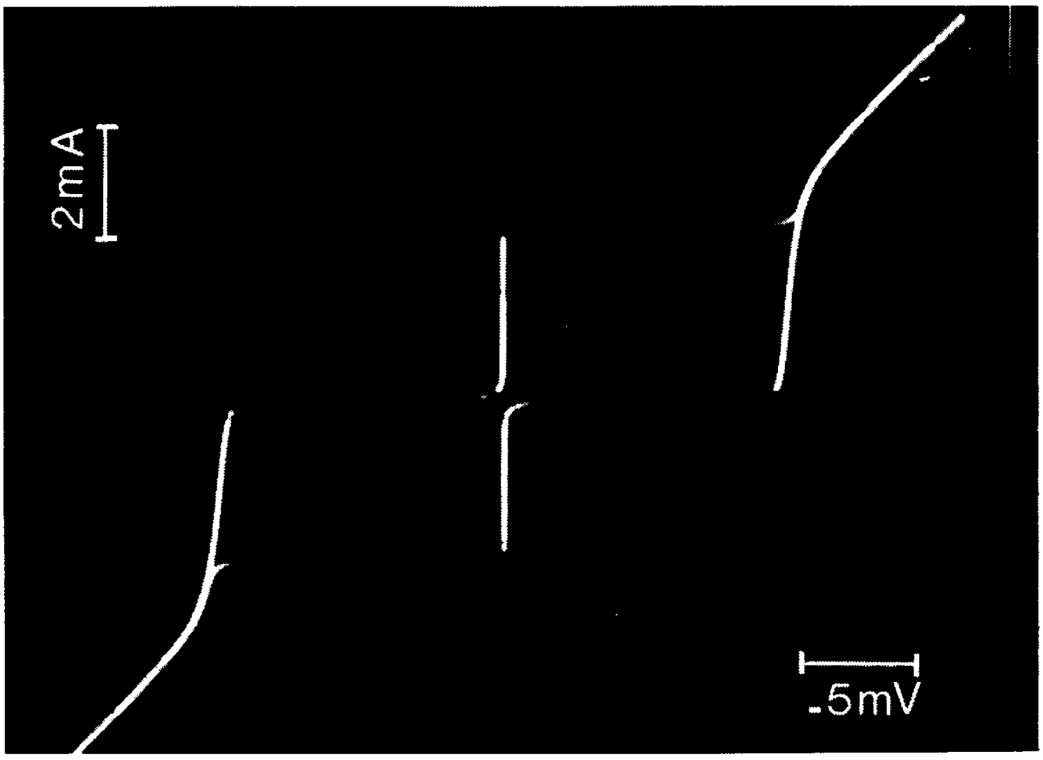

Figure 1.8: *I-V* characteristic of a Sn-Sn_xO_y-Sn Josephson junction at $T = 1.52$ K [12].

1.4.1 RCSJ model

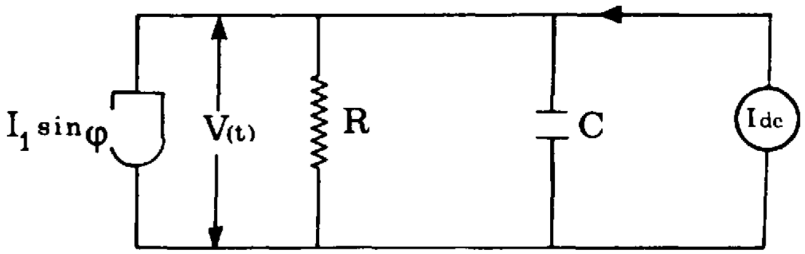

Figure 1.9: Equivalent circuit of a Josephson junction [12].

Even if the samples measured in this work are not Josephson junctions, the Josephson effect stays as a reference for whatever nanostructure or weak link may present effects related to the phase of the superconductor and its dynamics. For this reason it is important to study the resistively and capacitively shunted junction (RCSJ) model, which is commonly used to describe the phase dynamics. The current balance equation for the circuit in Figure 1.9 can be written as:

$$I_{dc} = C\frac{dV(t)}{dt} + \frac{1}{R}V(t) + I_1 \sin\varphi \quad . \tag{1.27}$$

Recalling the second Josephson equation and multiplying everything by $\hbar/2e$, the previous equation can be rewritten as:

$$\left(\frac{\hbar}{2e}\right)^2 C\frac{d^2\varphi(t)}{dt^2} + \left(\frac{\hbar}{2e}\right)^2 \frac{1}{R}\frac{d\varphi(t)}{dt} + \frac{\hbar}{2e}I_1 \sin\varphi - \frac{\hbar}{2e}I_{dc} = 0 \tag{1.28}$$

that can be seen like a motion equation for a "phase particle" moving in a potential:

$$m\frac{d^2\varphi(t)}{dt^2} + \eta\frac{d\varphi(t)}{dt} + \frac{\partial U}{\partial\psi} = 0 \tag{1.29}$$

where $m = \hbar^2 C/(2e^2)$ is the phase particle mass, $\eta = \hbar^2/(2e^2 R)$ is the damping coefficient and $U = -(\hbar/2e)(I_1 \cos\varphi + I\varphi)$ is the so-called *washboard potential*, shown in Figure 1.10.

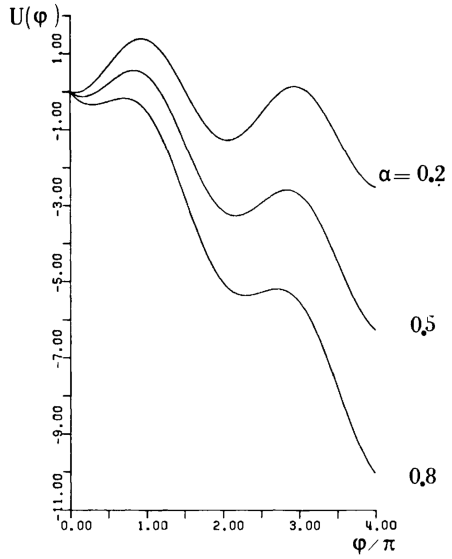

Figure 1.10: Washboard potential $U(\varphi)$ for different values of $\alpha = I/I_c$ [12].

A particle in the minimum of the washboard can have small oscillations with a frequency

$$\omega_P(I) = \left(\frac{2eI_c}{\hbar C}\right)\left(1 - \frac{I^2}{I_c^2}\right)^{1/4} = \omega_P(0)\left(1 - \frac{I^2}{I_c^2}\right)^{1/4} \tag{1.30}$$

The damping term can be rewritten as:

$$\eta = \frac{\hbar^2}{2e^2R} = \frac{\hbar}{2\pi}\frac{R_q}{R} \tag{1.31}$$

thus the damping is proportional to the normal conductance $G = 1/R$, where $R_q = h/(2e)^2$. The particle oscillations are confined in the minimum of the washboard potential, characterised by a barrier ΔU [23]:

$$\Delta U(I) = \frac{4\sqrt{2}}{3}\Phi_0 I\left(1 - \frac{I}{I_c}\right)^{3/2} \quad . \tag{1.32}$$

The particle can escape out of the barrier by thermal activation or quantum tunneling, as it will be explained in Section 1.6.

1.5 1D Superconductivity

Recently, superconductivity at the nanoscale is a key argument for fundamental science and nanostructures have become of great interest for their applications as

single-photon detectors [24–26]. How dissipation occurs in a confined geometry is a crucial key to understand superconductivity in these extreme conditions and obviously to engineer most of nanodevices.

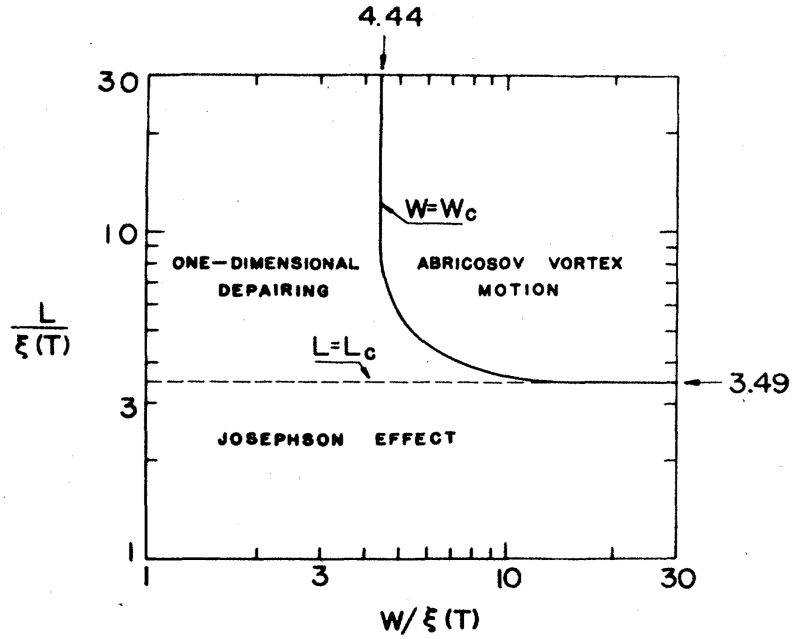

Figure 1.11: Superconducting regime in respect of length and width, normalised to the coherence length ξ. The solid line separates the regime where the vortices are free to move from the 1D-regime, in which 1D-instabilities affects the superconductivity. Under the dashed line, Josephson effect takes place [27].

The natural hystorical path to follow to describe dissipation in nanostructures originates from weak links, as highlighted in Figure 1.11, from Ref. [27], where it is shown how a bridge can turn into a Josephson junction by changing its dimensions. In other words a bridge composed of a single superconductor can behave as a Josephson junction when its length L is smaller than a few times the coherence length of the superconductor. For $L >> 3.5\,\xi$, no Josephson phenomena are observed. Depending on the width W the transition to the normal state will be driven by 1-D or 2-D processes, such as *phase slips* that are described below. Generally, following Ref. [28], a wire is considered a one dimensional system when its thickness d and width w are smaller than the coherence length ξ. This condition ensures the invariance of the order parameter across the wire, thus it can only evolve along it. In this thesis, Al nanowires [29–31] fall in the one-dimensional depairing region in Likharev's diagram, while NbTiN and NbN nanomeanders [26,32] fall in the Abrikosov vortex motion zone. The feasibility of 1D models and the

validity of Likharev's criterion on nanowires with different width and length has been proven in several studies [33, 34].
Al nanowires are characterised by a coherence length $\xi \sim 125\,\text{nm}$ that is greater than the cross-sectional dimensions ($d \sim 25\,\text{nm}$ and $w \sim 50\,\text{nm}$). It's interesting to note that even if the cross-sectional dimensions are not strictly minor than ξ, a nanowire can be consider a quasi-1D system if $(d, w) < \pi\sqrt{2}\xi$ [28]. Indeed, in this situation, vortices aren't stable in the wire and consequently the order parameter can be considered to vary only along the length of the wire. It is important to mention that, since the coherence length exceeds the cross-sectional dimensions, it is far larger than the Fermi wavelength λ_F of the electrons, thus the quasi-particle excitations are still bulk-like and their treatment is the one mentioned in Section 1.2 [28]. Nowadays, it is possible to fabricate wires as thick as $5\,nm$, that is a quasi-1D system in the limit of zero temperature for many materials, such as the aluminium [28]. Sometimes, it is also possible to consider a nanowire as a one dimensional system if its length is much larger than the other dimensions, i. e. $L >> (d, w)$ [11].
Since Al nanowires are more "standard" devices, they are used as terms of comparison for nanomeanders' results.

1.6 Phase Slips

In superconducting nanostructures, the transition from the superconducting state to the resistive state has been traditionally studied in terms of phase slips. Firstly Little [35] and later Langer and Ambegaokar [16] suggested that fluctuations of measured supercurrents from the mean field values were to be attributed to a phase slip of the complex order parameter. This phase slip, that can be due to either thermal or quantum fluctuations, causes a suppression of the order parameter magnitude, as shown in Figure 1.12b. It's interesting to note that the suppression length of the order parameter is $\sim \xi(T)$ [11].

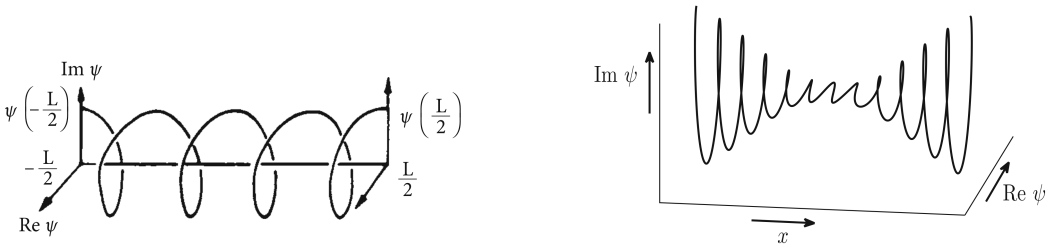

(a) (b)

Figure 1.12: Phase slip process: in (a) the real and imaginary part of ψ along the nanowire are reported in absence of a phase slip event; in (b) the amplitude suppression of the order parameter along the nanowire during a phase slip [11]. The phase slip core has a size comparable with ξ.

In their work, Langer and Ambegaokar took into consideration the case of a superconductor with $(d, w) < \xi$, i.e. a current biased 1D-nanowire whose Ginzburg-Landau free-energy functional is:

$$F - F_n = \int_{-L/2}^{L/2} A \left[a|\psi|^2 + \frac{b}{2}|\psi|^4 + \frac{\hbar^2}{4m} \left| \left(-\imath\nabla - \frac{2e}{\hbar c}\boldsymbol{A} \right) \psi \right|^2 \right] dx \tag{1.33}$$

where A is the cross-sectional area of the nanowire, L its length and F_n the free-energy of the normal state. Looking at Equation (1.33), it's easy to see that a phase slip, that is a discontinuity in $\varphi(x)$, would make the gradient to diverge: for this reason it is necessary an order parameter suppression, i.e. a local switch to the resistive state.
Following McCumber and Halperin [36], it's useful to consider the normalised order parameter

$$\Psi = \frac{\psi}{\sqrt{|a(T)|/b}} \,. \tag{1.34}$$

Rescaling the Equation (1.33) by the GL coherence length and an energy expressed in terms of the thermodynamic critical field

$$\xi(T) = \frac{\xi(0)}{\sqrt{1 - T/Tc}} \qquad H_c(T) = \sqrt{\frac{4\pi}{b}} a(T) \,,$$

it can be obtained the following equation:

$$F - F_n = AL\frac{H_c^2(T)}{4\pi}\int_{-L/2}^{L/2}\left\{-|\Psi|^2 + \frac{1}{2}|\Psi|^4 + \left|\left(-\imath\xi(T)\frac{d}{dx} - \xi(T)\frac{2e}{\hbar c}A_x\right)\Psi\right|^2\right\}\frac{dx}{L} \tag{1.35}$$

where, following the arguments reported in Section 1.3, $a(T) = A(T - T_c) = -|a(T)|$, since the nanostructure is below the critical temperature. Given this GL free-energy functional, the stationary solutions for the normalised order parameter can be found by solving the following equation:

$$(1 - |\Psi|^2)\Psi + \left(\xi(T)\frac{d}{dx} - \imath\xi(T)\frac{2e}{\hbar c}A_x\right)^2\Psi = 0 \quad . \tag{1.36}$$

In absence of an external magnetic field ($A_x = 0$), the general form for the normalised order parameter is

$$\Psi(x) = f(x)e^{i\varphi(x)} \tag{1.37}$$

which allows to separate the Equation (1.36) in two equations for magnitude $f(x)$ and phase $\varphi(x)$:

$$\begin{aligned} &\xi^2(T)\frac{d^2f}{dx^2} = -f + f^3 + \left(\frac{4}{27}\right)\frac{j^2}{f^3} \\ &\frac{dj}{dx} = 0 \ , \quad j = \frac{3\sqrt{3}}{2}f^2\xi(T)\frac{d\varphi}{dx} = \frac{3\sqrt{3}}{2}\kappa(1-\kappa^2) \end{aligned} \tag{1.38}$$

where $j = J/J_c$. The right-hand term of the first equation of the system can be rewritten as [16]:

$$-\frac{dU_{eff}}{df} = -f + f^3 + \left(\frac{4}{27}\right)\frac{j^2}{f^3} \Longrightarrow U_{eff} = \frac{1}{2}f^2 - \frac{1}{4}f^4 + \frac{2}{27}\frac{j^2}{f^2} \tag{1.39}$$

which remind the washboard potential of RCSJ model, as can be seen in Figure 1.13.

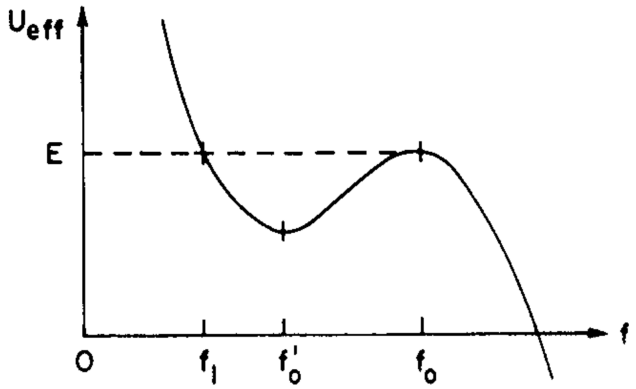

Figure 1.13: U_{eff} behaviour as a function of f with $J < J_c$ [16].

The Equations 1.38 can be solved in analogy with a mechanical system. Considering a particle of unit mass in a potential U_{eff}, whose radial and angular coordinates are respectively f and ϕ, and considering x as the time [16], the solution $\bar{\psi}$ for Equation (1.36) can be found. Replacing $\bar{\psi}$ in Equation (1.35), the free-energy barrier for a phase slip can be found as:

$$\Delta F^{-}(\kappa,T) = A\frac{H_c^2(T)}{\pi}\xi(T)\left[\frac{\sqrt{2}}{3}\sqrt{1-3\kappa^2} - \kappa(1-\kappa^2)\tan^{-1}\left(\frac{\sqrt{1-3\kappa^2}}{\sqrt{2}\kappa}\right)\right]$$
$$\Delta F^{+}(\kappa,T) = A\frac{H_c^2(T)}{\pi}\xi(T)\left\{\frac{\sqrt{2}}{3}\sqrt{1-3\kappa^2} + \kappa(1-\kappa^2)\left[\pi - \tan^{-1}\left(\frac{\sqrt{1-3\kappa^2}}{\sqrt{2}\kappa}\right)\right]\right\} \tag{1.40}$$

where ΔF^{+} stands for the uphill potential barrier (*anti-phase slip*) and the ΔF^{-} stands for the downhill potential barrier (*phase slip*). Following Ref. [37], the energy prefactor can be expressed as:

$$A\frac{H_c^2(T)}{\pi}\xi(T) = \frac{3\sqrt{3}}{8}\Phi_0 I_c(T) \quad . \tag{1.41}$$

In this way, it is possible to compute the barrier height without calculating the critical field $H_c(T)$.
Finally, to describe the dynamics of nanowires, it is useful to write the free-energy barrier of the phase slip (see Figure 1.13) as [38]:

$$\Delta F(I) = \sqrt{6} I_c \frac{\hbar}{2e}\left(1 - \frac{I}{I_c}\right)^{3/2} \quad . \tag{1.42}$$

1.6.1 Thermally activated phase slips

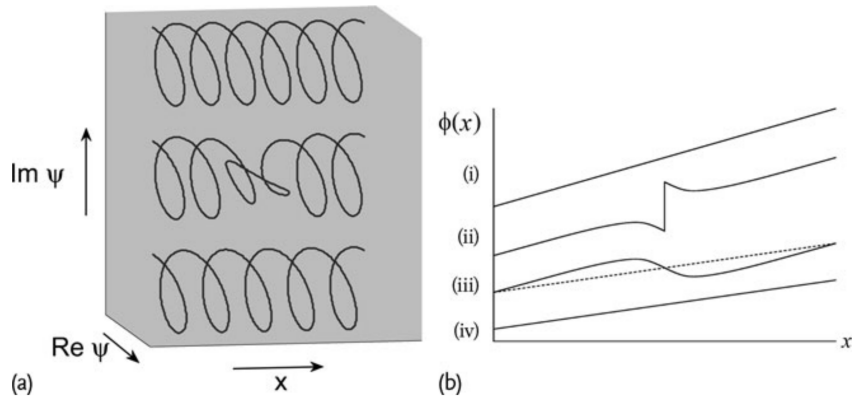

Figure 1.14: Phase slip dinamics: in (a) the variation of the ψ is shown. In the upper part there is the real and the imaginary part of the order parameter. After a phase slip, shown in the middle part of the figure, the ψ change: it has lost a winding. In (b) it is shown the same process, but only for the phase. Note that the slope of $\phi(x)$ in (iv) is different than in (i) [11].

In Figure 1.14, the physical mechanism of a thermally activated phase slip (TAPS) is described: in *(a)* the variation of the order parameter is presented; in *(b)* there is the variation of the phase through the nanowire due to a phase slip. Indeed, if the system is presumed to be in a local minimum of the potential, the thermal agitation makes the system oscillate enough to suddenly overcome the barrier. As the phase slip process is approached, the spatial region, wherein the 2π phase shift is located, is compressed and the point where the phase slip occurs has to be a zero for the order parameter. After the phase slip, the energy needed to overcome the potential barrier can be dissipated through the normal core generated by the phase slip.
The rate at which the phase (or anti-phase) slips occur is given by

$$\Gamma^{\pm} = \Omega_{\pm} \exp\left[\frac{-\Delta F^{\pm}}{k_b T}\right] \tag{1.43}$$

where the potential barrier gives an exponential suppression to the rate. The *attempt frequency* $\Omega_{\pm}$, that is the thermal agitation frequency, has been proposed by Langer and Ambegaokar [16] to be:

$$\Omega(T) = \frac{N_e}{\tau_e}$$

where N_e is the number of conduction electrons and $\tau_e \approx 10^{-12}\,\mathrm{s}$ is a typical relaxation time for electron scattering. Later on, McCumber and Halperin [36] estimated the attempt frequency within a TDGL theory (see Section 1.3.1), obtaining [11]:

$$\Omega(T) \sim \frac{L}{\xi(T)}\sqrt{\frac{\Delta F^{\pm}}{k_B T}} \times \frac{\text{entropy factor}}{\tau_{GL}}$$

where the first term is the number of the indipendent units for the phase slip process, the second one is associated with the number of energy phase space cells for this random process and the third is correlated to the characteristic relaxation time needed to explore the free-energy extrema during the process, given by the GL relaxation time (Equation (1.18)).
To achieve this form for $\Omega_{\pm}(T)$, it is necessary to make some assumptions to the TDGL theory previously presented [11]. Indeed, neglecting the vector potential, since the self-generated magnetic field is negligible, and the chemical potential, which can be ignored at this level of accuracy, the Equation (1.19) becomes

$$\frac{\partial \psi}{\partial t} = \frac{4\pi}{AH_c^2(T)\xi(t)\tau_{GL}(T)}\left[(1-|\psi|^2)\psi + \xi^2(T)\frac{\partial^2\psi}{\partial x^2}\right] \quad .$$

To take into account thermal fluctuations, a stochastic noise term should be added to the previous equation. Alternatively, following Ref. [36], Fokker-Planck equations can be used to determine the probability-density functional, from which it is possible to calculate the attempt frequency for phase $(-)$ and anti-phase $(+)$ slips:

$$\begin{aligned} \Omega_-(\kappa,T) &= (1-\sqrt{3}\kappa)^{15/4}(1+\kappa^2/4)\Omega(T) \\ \Omega_+(\kappa,T) &= \Omega(T) \end{aligned} \tag{1.44}$$

with

$$\Omega(T) = \frac{\sqrt{3}}{2\pi^{3/2}}\frac{L}{\xi(T)\tau(T)}\sqrt{\frac{\Delta F(T)}{k_B T}} \quad . \tag{1.45}$$

Taking into account Equation (1.40), it is possible to give an estimate of the escape rate for phase and anti-phase slip $\Gamma^{\pm}_{TAPS}(\kappa,T)$ in the Langer-Ambegaokar-McCumber-Halperin (LAMH) model

$$\Gamma^{\pm}_{TAPS}(\kappa,T) = \Omega_{\pm}\exp\left[-\frac{\Delta F^{\pm}(\kappa,T)}{k_B T}\right] \quad . \tag{1.46}$$

whereas the cumulative escape rate $\Gamma(\kappa,T)$ is given by

$$\Gamma_{TAPS}(\kappa,T) = \Gamma^{-}_{TAPS}(\kappa,T) - \Gamma^{+}_{TAPS}(\kappa,T) \tag{1.47}$$

However, the escape rate presented in Equation (1.46) is still not so easy to handle, so it is useful to rewrite the rate, following Ref. [30], as depending from the bias current I:

$$\Gamma_{TAPS}(T,I) = \frac{L}{\xi(T)\tau_{GL}}\sqrt{\frac{\Delta F(T,I)}{k_B T}}\exp\left[-\frac{\Delta F(T,I)}{k_B T}\right] \tag{1.48}$$

with

$$\Delta F(T,I) = \sqrt{6}\frac{\hbar}{2e}I_c(T)\left(1-\frac{I}{I_c(T)}\right)^{3/2} \tag{1.49}$$

It is important to note that such functional form allows to be not so accurate in the estimate of the attempt frequency, since minimal variations of the energy ratio would absorb all the inaccuracies of $\Omega(T)$. For the superconducting nanowires used as photon detectors, the escape rate gives an estimate of the dark counts rate of the detector, since the stochastic transition from the superconducting to the resistive state could give a false counting event.

Chapter 2

Switching Current Distributions

Superconducting nanostructures, in particoular meandered nanostrips, have acquired considerable interest as single photon detectors and for their use in quantum technologies. This is an additional reason to study the dissipation processes occuring during the current flow, since it can affect the dark counts rate in SNSPD. As it has been anticipated in Chapter 1, the dissipation in superconducting nanostructures is typically studied in the framework of thermally activated phase slip mechanism. Indeed, a nanostructure passes from the superconducting to the resistive state as a result of a phase slip event causing the local temperature increase due to Joule dissipation. This dynamics can be studied by measuring the critical current fluctuations, i. e. the switching current distributions, as it will be explained in Sections 2.1 and 2.2.
These distributions can give direct information on the phase dynamics and can be simulated by using a kinetic phase slip description, according to Refs. [37, 39]. Therefore, it has to be taken into account the heat generated in a phase slip process. The intrinsic stochasticity of a phase slip event is such that between two events, heating dissipation can affect the nanomeanders' behaviour and their transition to the resistive state. In particular, it has been used and developed a numerical method to simulate the nanostructure response to a current ramp, in order to reproduce the experimental results. At the end of this Chapter, the simulation algorithm will be depicted in some detail.

2.1 *I-V* Characteristics

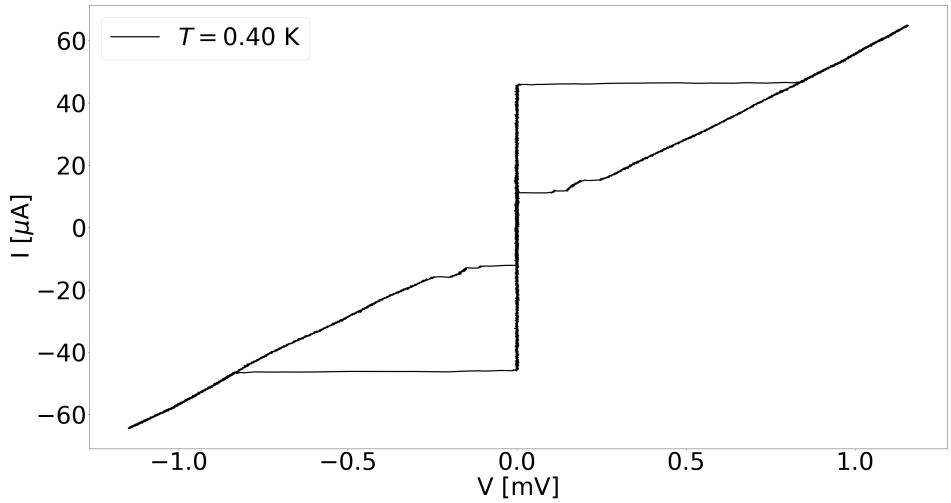

Figure 2.1: *I-V* characteristic of an Al nanowire at bath temperature $T = 0.4\,\mathrm{K}$.

In Figure 2.1, a typical *I-V* characteristic of a current biased Al nanowire is presented. Here, it is possible to distinguish the superconducting (S) branch, the normal state (N) branch and the retrapping (R) one, at which the transistion from N to S branch occurs. As the bias current increases, there is no voltage drop until it reaches a critical value, called switching current I_{sw}. At I_{sw}, a jump to a finite voltage state occurs as the system passes to the N-branch. The switching current is a stochastic event, i.e. measurements done under the same experimental conditions don't have the same switching current, since fluctuations play a relevant role.
Thus, the stochastic switching from the superconducting to the resistive state can be studied in terms of phase fluctuations, as described in Section 1.6. As a matter of fact, the voltage depends on the phase slip rate (or escape rate) Γ, according to the relation [11]:

$$V = \frac{2\pi\hbar}{2e}[\Gamma^- - \Gamma^+] \quad . \tag{2.1}$$

A single phase slip event can be observed only when the induced heat is such that the phase slip core reaches a temperature larger than its critical temperature, causing the transition to the normal state [28]. This occurs mainly for temperatures significantly lower than T_c.

2.2 Kurkijärvi-Fulton-Dunkleberg Transformations

The statistical analysis of the switching current distributions (SCDs) has been carried out by Kurkijärvi, Fulton and Dunkleberg [40, 41] on standard tunnel Josephson junctions and later adapted to study the critical current fluctuations of superconducting nanodevices. Actually, Kurkijärvi theory is about every stochastic switching event distribution, but here it will be presented in relation to SCD for a current-biased nanowire. In the phase slip framework, the Kurkijärvi theory can be applied only in phase slip processes involving single events.
Thus, let's consider the bias current slowly increasing. When $I < I_c$ the phase particle is trapped in the potential well, which disappears as the current reaches its critical value I_c and then the transition to the resistive state occurs. The phase particle can overcome the free-energy barrier, due to thermal fluctuations, for values of the bias current lower than I_c. The current ramp has to be as slow as possible, to allow the system to relax, and its slope $\Delta I/\Delta t$ has to be as much as possible constant. After the resistive jump the current is rapidly decreased in order to reach the superconducting state. Repeating this procedure a large number N of times, usually $N = 5\,000$, a distribution for the switching current values can be derived. An example of SCD with the area normalised to 1 is reported in Figure 2.2

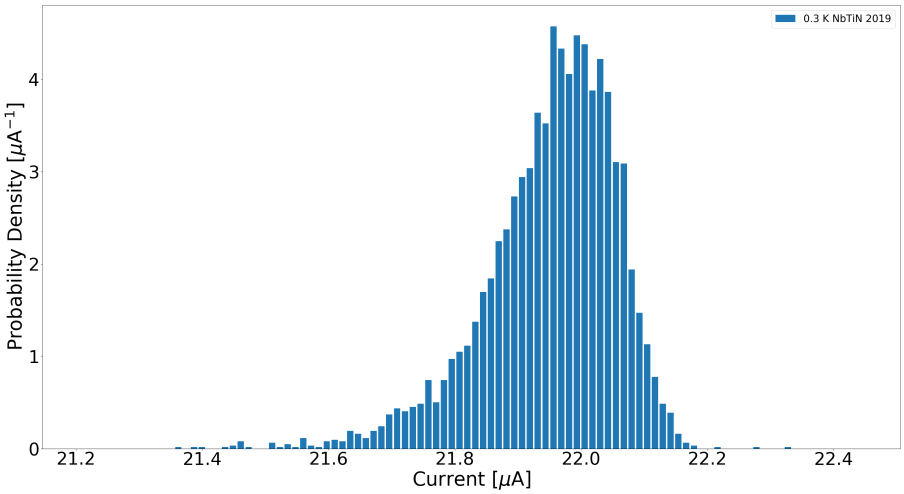

Figure 2.2: Switching current distribution with the area normalised to 1 measured on a NbTiN nanomeander at $T = 0.3\,\mathrm{K}$

From the measured SCD, the momenta of the distribution can de determined. The mean switching current $\langle I_{sw} \rangle$, standard deviation σ and skewness $\tilde{\mu}_3$ can be

defined:

$$\langle I_{sw}\rangle = \sum_k^N P_k I_k \qquad \sigma = \sqrt{\sum_k^N P_k (I_k - \langle I_{sw}\rangle)^2}$$
$$\tilde{\mu}_3 = \frac{\sum_k^N P_k (I_k - \langle I_{sw}\rangle)^3}{\sigma^3}$$

where $P_k = N_k/N$, with $\sum_k N_k = N$ the numbers of events for I_k. The standard deviation σ gives information about the distribution width, whereas the skewness $\tilde{\mu}_3$ is a measurement of the lack of symmetry. As it can be seen in Figure 2.2, SCDs are asymmetric, showing a longer tail on the left and for this reason a skewness $\tilde{\mu}_3 \approx -1$ [28]. For the sake of comparison, a Gaussian distribution is characterised by a skewness $\tilde{\mu}_3 = 0$.
Kurkijärvi found a temperature and current dependence for the standard deviation

$$\sigma(T, I_c) \propto T^{2/3} I_c^{1/3} \tag{2.2}$$

that is called *Kurkijärvi power law* for standard deviation [28].
Assuming the ergodic hypotesis, it can be said that N measurements of the same system should give the same results of a single measurement on N systems under the same conditions At time $t = 0$, all the N nanowires are in the superconducting state. Later on, when $I = I(t)$ is applied, N_1 nanowires are in the superconducting state and N_2 are in the normal state: obviously N_2 increases as the current approaches the critical value I_c, i.e. as the time increases. Thus, in an interval dI, N_2 increments of $dN_2 = N_2(I + dI) - N_2(I)$ and the probability of a nanowire to switch to the normal state is given by the equation

$$P(I)dI = \frac{dN_2}{N} \tag{2.3}$$

and, keeping in mind $N = N_1 + N_2$,

$$dN_1 = -NP(I)dI = -NP(I)\nu dt \quad . \tag{2.4}$$

where $\nu = dI/dt$ is the current ramp rate. Equation (2.4) can be solved, giving

$$N_1(I) = N\left[1 - \int_0^I P(I')dI'\right] \tag{2.5}$$

However, in absence of thermal fluctuations, the probability density is Dirac delta function, $P(I) = \delta(I - I_c)$. Instead, fluctuations have to be considered and thus the escape rate Γ has to be introduced. Indeed, as seen in Section 1.6, Γdt is

the number of phase slips in the time interval dt. The number of the unswitched nanowires is

$$dN_1 = -N_1 \Gamma dt \quad . \tag{2.6}$$

Keeping in mind $N_1(0) = N$, the Equation (2.6) can be solved, giving

$$N_1(t) = N \exp\left[-\int_0^t \Gamma(I(t'))dt'\right] \quad . \tag{2.7}$$

Equating (2.4) and (2.6) and considering Equation (2.5), the escape rate in terms of the probability density is given by

$$\begin{aligned}\Gamma(I) =& P(I)\nu\left[1 - \int_0^I P(I')dI'\right]^{-1} = P(I)\nu\left[\int_I^{I_c} P(I')dI'\right]^{-1} = \\ &- \nu\frac{d}{dI}\left[\ln\int_I^{I_c} P(I')dI'\right]\end{aligned} \tag{2.8}$$

that is called *Kurkijärvi-Fulton-Dunkleberg (KFD) transformation* [28].
The probability density extrapolated from the data is discrete, thus a discrete KFD transformation has to be find. Actually, if the distribution bin has a fixed size ΔI, the discrete value of the probability density P_k can be seen as an average of $P(I)$ over the bin size

$$P_k \equiv \frac{1}{\Delta I}\int_{I_k - \Delta I/2}^{I_k + \Delta I/2} P(I')dI' \tag{2.9}$$

where $I_k = I_{Max} - (k - 1/2)\Delta I$ is the measured switching current value, I_{Max} is the maximum switching current measured [41]. Note that the I_1 is the maximum value for I_k.
Remembering that $\Gamma = -\nu dZ/dI$, where $Z = \int_I^{I_c} P(I')dI'$, the discrete escape rate can be written as [28]:

$$\Gamma(I_k) = -\nu\left.\frac{dZ'}{dI}\right|_{I=I_k} \quad . \tag{2.10}$$

Looking at the derivative term in Equation (2.10), it can be noticed that

$$\left.\frac{d(\ln Z)}{dI}\right|_{I=I_k} \longrightarrow -\frac{\ln Z_k - \ln Z_{k-1}}{\Delta I} = \frac{1}{\Delta I}\ln\frac{Z_{k-1}}{Z_k} \tag{2.11}$$

where $Z_k \equiv Z(I_k)$. By implementing Equation (2.11) in Equation (2.10), the discrete escape rate can be rewritten as

$$\Gamma(I_k) = \frac{\nu}{\Delta I} \ln \frac{Z_k}{Z_{k-1}} \quad .$$

Defining Z_k as the sum of short-segments integrals

$$Z_k = \int_{I_k}^{I_c} P(I')dI' = \sum_{l=1}^{l=k} \int_{I_l-\Delta I/2}^{I_l+\Delta I/2} P(I')dI' = \Delta I \sum_{l=1}^{l=k} P_l \quad ,$$

it is possible to express the *discrete KFD transformation* as [28, 41]:

$$\Gamma(I_k) = \frac{\nu}{\Delta I} \ln \frac{\sum_{l=1}^{l=k} P_l}{\sum_{l=1}^{l=k-1} P_l} = \frac{\nu}{\Delta I} \ln \left(1 + \frac{P(I_k)}{\sum_{l=1}^{l=k-1} P(I_l)} \right) \quad . \tag{2.12}$$

2.2.1 Inverse KFD transformation

For superconduting devices, the escape rate from the superconducting to the resistive state can be expressed in the form of the Arrhenius law:

$$\Gamma = Ae^{-BT} \quad -$$

In general, it is useful to find an inverse relation between $P(I)$ and the escape rate. Indeed, integrating Equation (2.6), it can be obtained

$$N_1(t) = N \exp \left[- \int_0^t \Gamma(I(t'))dt' \right] \quad . \tag{2.13}$$

Thus, equating Equations (2.4) and (2.6)

$$N_1\Gamma = N\Gamma \exp \left[- \int_0^t \Gamma(I(t'))dt' \right] = NP(I)\nu$$

where in the mid-term N_1 has been replaced with Equation (2.13). In this way, an *inverse KFD transformation* can be expressed as [28]

$$P(I) = \frac{\Gamma(I)}{\nu} \exp \left[-\frac{1}{\nu} \int_0^I \Gamma(I')dI' \right] \quad . \tag{2.14}$$

Actually, since $P(I_k)$ are directly measured, Equation (2.14) can be used to fit the probability density $P(I)$, once the escape rate of a specific dissipation process is known. In the following, the escape rate derived for thermal phase slips will be considered.

2.3 Local Heat Dynamics

In the previous Section, the standard relations between the probability density and the escape rate in the switching process to the resistive state have been derived. As mentioned before, KFD and inverse KFD transformations resulted from the dynamics of standard tunnel Josephson junctions. In superconducting nanostructures, high values of the critical current density are often achieved, of the order of $10^6 \mathrm{A/cm}^2$ [24]. In this case, switching to the resistive state leads to a local temperature increase, which can be described in terms of Joule dissipation through the nanostructure [37,39]. Hence, the switching current distributions can be simulated studying the local heat dynamics of the nanowire, under the assumption that a switching event occurs when the phase slips give such energy that the phase slip (PS) core temperature is increased over a threshold temperature T_{th}.
For this reason, a model is needed to describe the heat dynamics of phase slips. The model proposed in Refs. [37, 39] considers a nanowire of length L suspended between two thermal baths, as shown in Figure 2.3a. In this way, the only available cooling mechanism to dissipate Joule heating is the conduction of heat from the center of the wire to its ends. It's important to notice that the wire length L can be slightly different from the real geometric length, to compensate the heat spread in the leads at bonding point. It is assumed that the system is in the dirty limit, which means electron mean free-path is much shorter than coherence length.

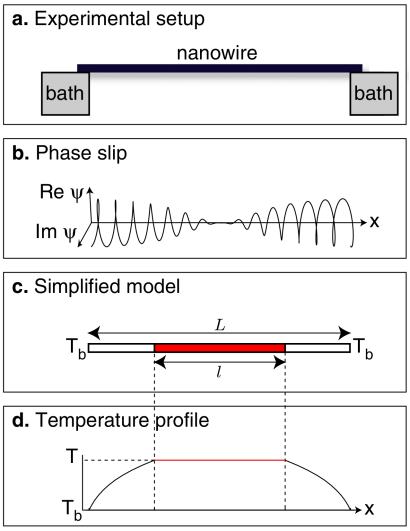

Figure 2.3: In the panel (a) the sketch of a typical experiment setup is presented. In (b) there is shown the real and imaginary part of the order parameter along the wire. In (c) the simplified model is shown. In (d) there is presented the temperature profile along the wire [39].

Since the heat generated locally in the nanostructure can flow away only through the ends, the static heat equation describing the wire heating and cooling is [37]

$$Q_{source}(x) = -\partial_x[K_s(\Theta)\partial_x(\Theta(x))] = -\frac{\partial K_s}{\partial \Theta}(\partial_x \Theta)^2 - K_s(\Theta)\partial_x^2\Theta \tag{2.15}$$

where $\Theta(x)$ is the nanowire temperature at position x and $K_s(\Theta)$ is the thermal conductivity. In addiction to Eq. 2.15, boundary conditions $\Theta(\pm L/2) = T_b$ are needed to take into account the presence of the bath at the ends of the wire. The power per unit volume dissipated via Joule effect Q_{source} can be expressed as:

$$Q_{source} = \frac{I^2 R(\Theta(x), I)}{AL} \tag{2.16}$$

where $R(\Theta(x), I)$ is the entire nanowire resistance at the uniform temperature $\Theta(x) = \Theta'$, A is the cross-sectional area and L is the wire length. Keeping in mind the second Josephson equation and Equation (2.1), the resistance can be written as

$$R(\Theta(x), I) = \frac{V}{I} = \frac{1}{I}\frac{\Phi_0}{2\pi}\frac{d\phi}{dt} = \frac{\Phi_0 \Gamma(\Theta, I)}{I} \tag{2.17}$$

and then, Equation (2.16) can be rewritten as

$$Q_{source} = \frac{I\Phi_0 \Gamma(\Theta, I)}{AL} \tag{2.18}$$

where $\Gamma \equiv \Gamma_- - \Gamma_+$, as defined in Section 1.6. Hence, recalling the heat continuty equation:

$$\nabla \cdot j_Q + \partial_t Q = Q_{source}$$

where the heat current j_Q is defined as

$$j_Q \equiv -K_s \nabla \cdot \Theta \tag{2.19}$$

and the energy density Q is

$$Q = \int_0^{\Theta(x)} C_v(\Theta') d\Theta' \quad ; \tag{2.20}$$

it's possible to derive the time-dependent heat equation:

$$C_v(\Theta)\partial_t \Theta(x,t) = \partial_x[K_s(\Theta)\partial_x \Theta(x,t)] + Q_{source} \tag{2.21}$$

where C_v is the wire specific heat.
By assuming the Joule heating caused by single phase slips, Q_{source} can be rewritten in a discrete form as

$$Q_{source}(x,t) = \frac{W_{ps}}{A}\sum_i \sigma_i F(x - x_i)\delta(t - t_i) \tag{2.22}$$

where we are considering discrete phase slip events that occur at random time t_i and position x_i, with $F(x-x_i)$ as a spatial form factor of unit weight, which gives the information about the spatial distribution of the heat, and $\sigma_i = \pm 1$ for phase or antiphase slips. W_{ps} is the energy of a single phase slip defined by

$$W_{ps} = \int IV dt = I \int_0^{2\pi} \frac{\hbar}{2e} d\phi = I\Phi_0 \quad . \tag{2.23}$$

Thus, using Equation (2.22) in Equation (2.21), it can be obtained a stochastic Langevin equation with a "noise" term distinctive of the temperature jump.
Therefore, Equation (2.21) can be used to investigate the superconducting-resistive transition, but the presence of both temporal and spatial randomness makes it very hard to handle. For this reason, in Refs. [37,39], some assumptions are made. First of all, because there are the two thermal baths at the edge of the nanostructure, it's assumed that the phase slips occur mainly in the central part of the nanowire, heating a region of length $l \sim \xi(T)$, which is at a uniform temperature T, as shown in Figure 2.3c-d. In this way, the heat flows away through the end segments of length $(L-l)/2$, whose heat capacity will be ignored. Then, neglecting the antiphase slips, since for bias currents close to I_c their probability is quite low, it is possible to write a stochastic ordinary differential equation for the time evolution of the PS core's temperature

$$\frac{dT}{dt} = -\alpha(T, T_b)(T - T_b) + \eta(T, I) \sum_i \delta(t - t_i) \tag{2.24}$$

where the first term on the right represents the deterministic coolig and the second one the stochastic heating due to phase slip [37, 39].
To understand as deeply as possible the local heating dynamics, making a comparison between Eq. 2.16 and Eq. 2.22, the simplified model can be written in a continuous way:

$$\frac{dT}{dt} = -\alpha(T, T_b)(T - T_b) + \eta(T, I)\Gamma(T, I) = -\frac{\partial U(T, I)}{\partial T} \tag{2.25}$$

that can be seen like a motion equation of an overdamped "particle" of position $T(t)$ in a fictitious effective potential $U(T, I)$, whose behaviour as a function of T and I is shown in Figures 2.4a and 2.4b.

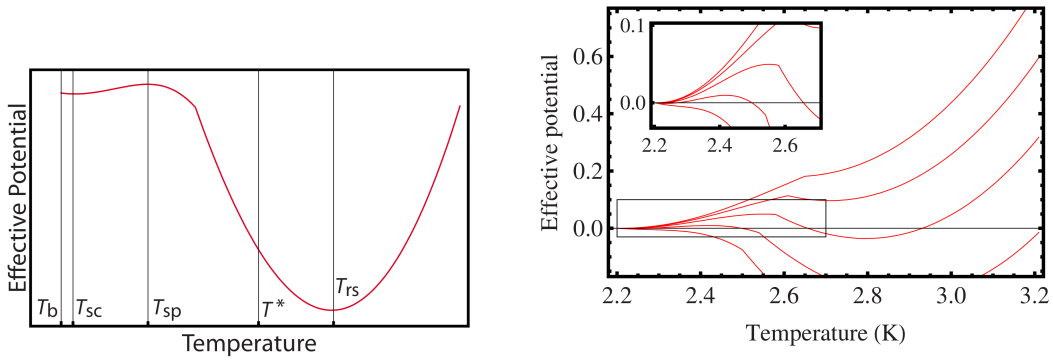

(a) (b)

Figure 2.4: Effective potential pointed out in Equation (2.25). In (a) $U(T, I)$ at a fixed I. Several temperatures can be noted: T_{sc} is the temperature for the minimum of $U(T)$ in the superconducting state; T_{rs} is for the minimum in the resistive state; T_b is the bath temperature. In (b) $U(T, I)$ behaviours for different bias current values (0.175, 0.195, 0.215, 0.235, 0.255 μA). In the inset the local maximum are shown. [37].

In Figure 2.4a it is possible to distinguish two critical points of the effective potential $U(T, I)$. Indeed, the system is in a bistable state: it can be either superconducting or in a resistive state. As the current is low, which situation is the upper curves in Figure 2.4b, there is only the superconducting minimum at T_{sc}, since the system cannot be in a normal phase. Increasing the bias current, a second minimum develops at T_{rs}, in which the system is in the resistive state, as it can be seen in lower curves in Figure 2.4b. Thus, at the same value of bias current, the system can stay either in the superconducting or normal state. If the temperature rise is smaller than the difference between the two minima, the system remains in whichever minimum it was [37].
To better understand the heat dynamics, it is important to clarify the meaning of the stochastic heating and deterministic cooling terms.

2.3.1 Stochastic heating

As the phase slip occurs, the thermal "jump" $\eta(T, I)$ of the central segment l can be found solving the integral equation:

$$\Phi_0 I = Al \int_{T_i}^{T_i+\eta(T,I)} C_v(T')dT' \quad , \tag{2.26}$$

where $\eta(T, I) = T_f - T_i$. The left hand term is the energy of a single phase slip, see Equation (2.23). To bear in mind that not all the cross-sectional area passes

from the superconducting to the resistive state, it is assumed the specific heat to be a weighted average of its BCS and Fermi liquid limits [42]:

$$C_v(T) = \frac{A_{BCS}C_{v_{BCS}}(T) + A_{FL}C_{v_{FL}}(T)}{A} \tag{2.27}$$

where A_{BCS} and A_{FL} are superconducting and normal cross-sectional areas, for which it is valid the constitutive relation $A = A_{BCS} + A_{FL}$.
The specific heat of a Fermi liquid $C_{v_{FL}}$ can be written as [10]:

$$C_{v_{FL}}(T) = \frac{2}{3}\pi^2 k_B^2 N_0 T \tag{2.28}$$

where N_0 is the density of state per unit volume at the Fermi level. Following Ref. [43], the specific heat of a superconductor $C_{v_{BCS}}$ can be defined with respect to $C_{v_{FL}}(T_c)$ as:

$$\frac{C_{v_{BCS}}(T)}{C_{v_{FL}}(T_c)} = \begin{cases} \dfrac{3\sqrt{2}}{\pi}\exp\left[-\dfrac{1}{\tau}\left(\tau^{-3/2} + \dfrac{3}{2}\tau^{-1/2} + 2\tau^{1/2} + \tau^{3/2}\right)\right] & \text{for } \tau \in [0, 0.35] \\ -0.86\tau + 3.560\tau^2 & \text{for } \tau \in]0.35, 0.65] \\ 2.43\tau(+0.936\log\tau) & \text{for } \tau \in]0.65, 1] \end{cases} \tag{2.29}$$

where $\tau = T/T_c$.

2.3.2 Deterministic cooling

The thermal relaxation term can be found equating the heat currents, as defined in Equation (2.19) and it can be written as

$$\alpha(T, T_b) = \frac{4}{l(L-l)C_v(T)}\frac{1}{T - Tb}\int_{T_b}^{T} K_s(x)dx \quad . \tag{2.30}$$

In analogy with $C_v(T)$, K_s has to be written as a weighted average of its BCS and Fermi liquid limits:

$$K_s(T) = \frac{A_{BCS}K_{s_{BCS}}(T) + A_{FL}K_{s_{FL}}(T)}{A} \tag{2.31}$$

For a Fermi liquid, the thermal conductivity is [44, 45]

$$K_{s_{FL}} = \frac{\pi^2 k_B^2}{3e^2}\frac{LT}{AR_N}$$

where R_N is the normal resistance of the nanowire. For a superconductor, instead, the thermal conductivity is given by:

$$K_{s_{BCS}} = 2N_0 D k_B^2 T \int_{\Delta/k_B T}^{\infty} \frac{1}{2} sech^2(x) x^2 dx$$

where D is the diffusion constant of the material and Δ is the superconducting gap. Taking into account the previous equations, the total thermal conductivity K_s is:

$$K_s(T) = 2\tilde{A}_{BCS} N_0 D k_B^2 T \int_{\Delta/k_B T}^{\infty} \frac{1}{2} sech^2(x) x^2 dx + \tilde{A}_{FL} \frac{\pi^2 k_B^2}{3e^2} \frac{LT}{AR_N} \tag{2.32}$$

where $\tilde{A}_i = A_i/A$. Therefore, in Equation (2.30), the contribution due to the thermal conductivity can be written in the following way:

$$\begin{aligned}
\int_{T_b}^{T} K_s(x)dx &= 2\tilde{A}_{BCS} N_0 D k_B^2 \int_{T_B}^{T} y \int_{\Delta/k_B y}^{\infty} \frac{1}{2} sech^2(x) x^2 dx dy + \tilde{A}_{FL} \frac{\pi^2 k_B^2}{3e^2} \frac{L}{AR_N} (T^2 - T_b^2) = \\
&= 2\tilde{A}_{BCS} N_0 D k_B^2 T_c^2 \Xi + \tilde{A}_{FL} \frac{\pi^2 k_B^2}{6e^2} \frac{L}{AR_N} (T^2 - T_b^2) = \\
&= 2\tilde{A}_{BCS} N_0 D k_B^2 T_c^2 \Xi + \tilde{A}_{FL} \frac{\pi^2}{6r_n} \frac{k_B^2 L}{Ah} (T^2 - T_b^2)
\end{aligned}$$

where $r_n = R_N(e^2/h)$ is the dimensionless resistance and the number Ξ is:

$$\begin{aligned}
\Xi &= \frac{1}{T_c^2} \int_{T_b}^{T} y \int_{\Delta/k_B y}^{\infty} \frac{1}{2} sech^2(x) x^2 dx dy = \\
&= \frac{1}{2T_c^2} \int_{T_b}^{T} \left[-8\mathrm{Li}_2 \left(\sinh\left(\frac{k_B y}{\Delta}\right) - \cosh\left(\frac{k_B y}{\Delta}\right) \right) + \right. \\
&\left. + 2\frac{k_B y}{\Delta} \left(\frac{k_B y}{\Delta} + 4\log\left(1 + e^{\frac{-k_B y}{\Delta}}\right) \right) - \frac{k_B y}{\Delta} \tanh\left(\frac{k_B y}{2\Delta}\right) \right] \frac{\Delta}{k_B y} dy
\end{aligned}$$

where $\mathrm{Li}_2(z)$ is the dilogarithm of the complex number z.
Thus, Eq. 2.30 can be written as

$$\alpha(T, T_b) = \frac{4}{l(L-l)} \frac{1}{k_B(T - T_b)} \frac{2\tilde{A}_{BCS} N_0 D k_B^2 T_c^2 \Xi + \tilde{A}_{FL} \frac{\pi^2}{6r_n} \frac{k_B^2 L}{Ah} (T^2 - T_b^2)}{C_v(T)/k_B} \tag{2.33}$$

At fixed bias current, the system is at $T = T_b$ and the temperature of the central region of the nanowire cannot change, until a phase slip occurs, which induces a thermal jump η. If a single thermal jump is not sufficient to induce the switching

and multiple phase slips are needed, it can happen that between two thermal jumps there is a transient in which only the cooling term acts. In Figure 2.5, a typical simulation is shown.

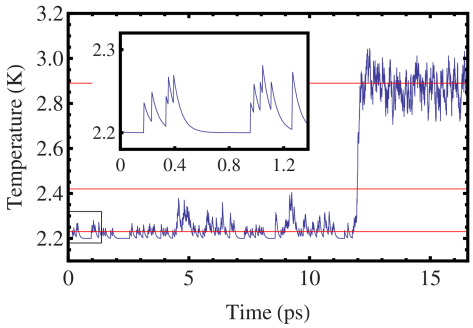

Figure 2.5: Temperature dynamics of a nanowire, where the peaks are the thermal jumps and the relaxation is due to deterministic cooling [37].

2.4 Simulation process

The model presented in Section 2.3 can be used to simulate the measured SCDs. The Python programm used to implement this model has been realised in collaboration with professor Procolo Lucignano[1].
A bias current ramp is introduced through a constant increasing step, which is determined by setting the critical current $I_c(T)$. At the beginning of the simulation, the system is at bath temperature T_b, which is a given parameter. The deterministic cooling term gives no contribution and the righ-hand term of Equation (2.24) does not give any contribution to the temperature until a thermal jump η occurs. If the thermal jump is sufficient to overcome the threshold temperature T_{th}, the system can be considered switched to the resistive state. On the other hand, if after the phase slip $T' < T_{th}$, the systems persists in its superconducting state at a T' temperature carrying a slightly higher current. An example of temperature dynamics is shown in Figure 2.5 to represent its complexity. The systems may cool down from its previous state until another phase slip event occurs. This process continues until the threshold temperature is overcome and the system switches to the resistive state. At low temperatures, the specific heat is quite low, because the nanowire is deeply in the superconducting state: for this reason a single phase slip, i.e. a single thermal jump η is enough to get the system into the resistive state. As the temperature increases, the specific heat increases and more jumps

[1]Dipartimento di Fisica, Università di Napoli 'Federico II', Monte Sant'Angelo, I-80126 Napoli, It

are needed to reach the second minimum of the potential in Eq. 2.25, as shown in Figure 2.5. To simulate the stochasticity of a phase slip, a random number $r \in [0, 1]$ is compared with the theoretical $\Gamma(T, I)$ value:

- If $r > \Gamma(T, I)$:
$$\frac{dT}{dt} = -\alpha(T, T_b)(T - T_b)$$
- If $r \leq \Gamma(T, I)$:
$$\frac{dT}{dt} = -\alpha(T, T_b)(T - T_b) + \eta(T, I)$$

$\Gamma(T, I)$ gives a measure of the probability of a single thermal jump occurence [11, 28, 37, 39]. For low bias currents, the condition $\Gamma(T, I) << 1$ always holds, it is very likely that the random number r would be greather than $\Gamma(T, I)$. On the other hand, for higher bias currents the condition $\Gamma(T, I) >> 1$ holds and therefore the second condition takes place and thermal jumps occur. Simulating this process for a reasonably high number of times N (see below), a distribution of the events, which bring the system from the S to the N state, can be obtained. In this thesis, the results presented in Chapter 4 have been obtained with $N = 4000$ events and only the thermally activated phase slip escape rate Γ has been considered (see Section 1.6.1). Indeed, the distributions are obtained even for lower values of N, but in order to fit the experimental data, it has been choosen a number of events close to the one collected for the measured SCDs, which is $N = 5000$ (see Section 3.4). From now on, phase slips are the only thermal events that will be considered in the superconducting to resistive state transition. Indeed, no significant differences are expected in preferring an alternative model to the TAPS in the local heat dynamics and, in the majority of the escape rate models, Γ has an Arrhenius law form, which is the same expected from the LAMH model.
T, I_c and T_{th} are the significant parameters involved in these simulations. As it will be clear from the comparison with the experiments, these quantities are not completely free parameters, since experimental conditions fix their range of values. Other parameters, such as the diffusion constant and the geometrical dimensions, are considered fixed for each sample [29].
The temperature T obviously modifies the position and the shape of the SCDs in an impressive way, as shown in Figure 2.6 and discussed below. Nevertheless in some sense, when fitting a series of measurements at different temperatures (see Chapter 4), T turns as not a completely free fitting parameter and acts as self-consistent check for the whole physical picture.

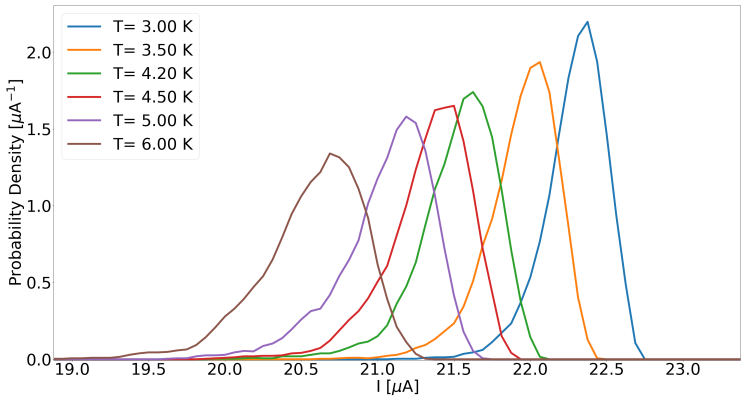

Figure 2.6: Simulated SCDs at different temperatures are presented, with $I_c = 25\,\mu\text{A}$ and $\Delta T = T_{th} - T = 0.11\,\text{K}$.

Simulations in Figure 2.6 have been done in the single phase slip regime, in which only the stochastic heating is involved (Section 2.3.1), fixing I_c and T_{th}. As the temperature decreases, the distribution has a minor width and an increasing mean switching current, as shown in Figures 2.7a and 2.7b.

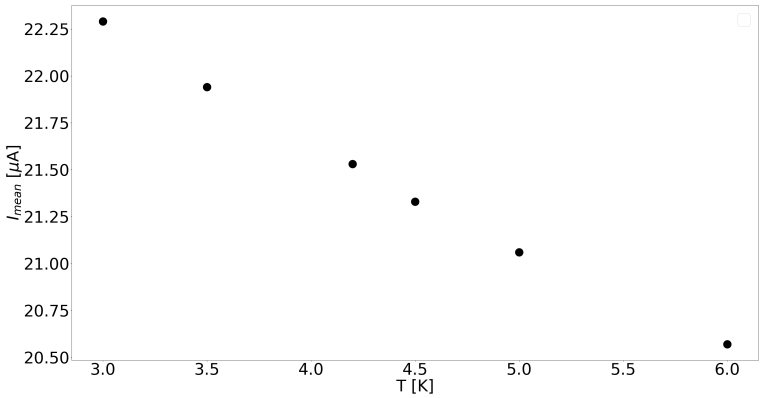

(a)

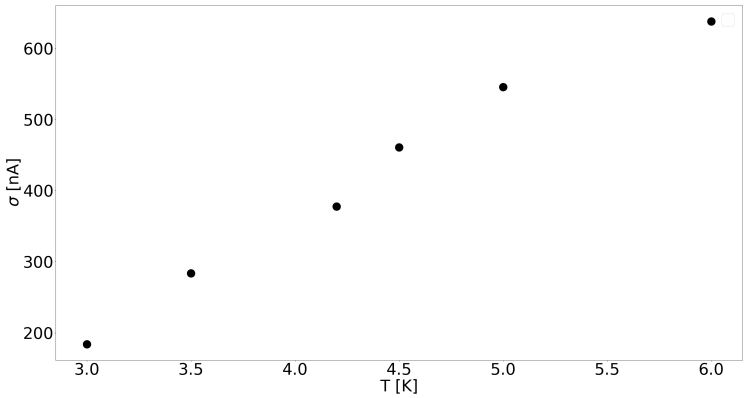

(b)

Figure 2.7: Simulated mean switching currents and standard deviation σ as function of temperature T.

At high temperature, thermal fluctuations affect the switching current values, causing premature switching transitions, as it can be seen from the I-V characteristics [46]. Thus, σ increse is proportional to the temperature, as predicted by Equation (2.2), and the $\langle I_{sw} \rangle$ consequently decreases. In the multiple phase slip processes, the behaviour of σ is very different and the distribution shape depends on the threshold temperature T_{th}.
In these processes where multiple phase slips are involved, the deterministic cooling (Section 2.3.2) plays a relevant role in the simulation, allowing to fit the measured SCDs by tuning the threshold temperature T_{th}, as shown in Figure 2.8.

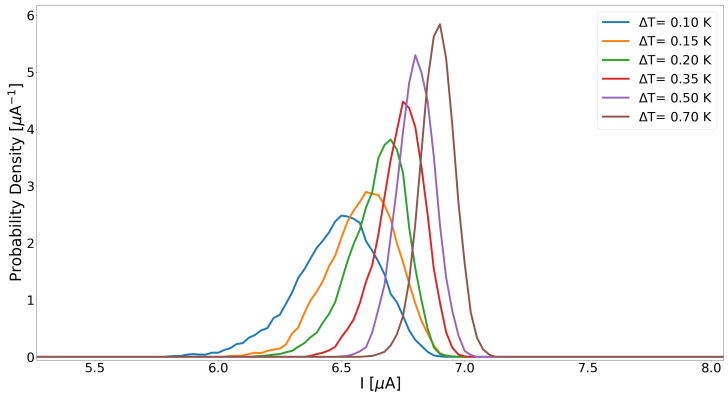

Figure 2.8: Simulated SCDs with different values of threshold temperature are presented, whose values are indicated in relation with the temperature ΔT. In these simulations I_c has been fixed at $10\,\mu$A and $T = 6\,$K.

As the threshold temperature increases, higher values of the critical current are needed to make the switching event to happen and σ decreases. Following Ref. [39], a possible explaination is that as the number of events necessary to switch from the superconducting to the resistive state increases, the stochasticity of the switching event drops and consequently the standard deviation σ is smaller. Indeed, looking at the behaviour of the mean number of phase slips as a function of temperature T in Figure 2.9, the PSs necessary to make the transistion to happen increase as the threshold temperature increases and thus as σ decreases.

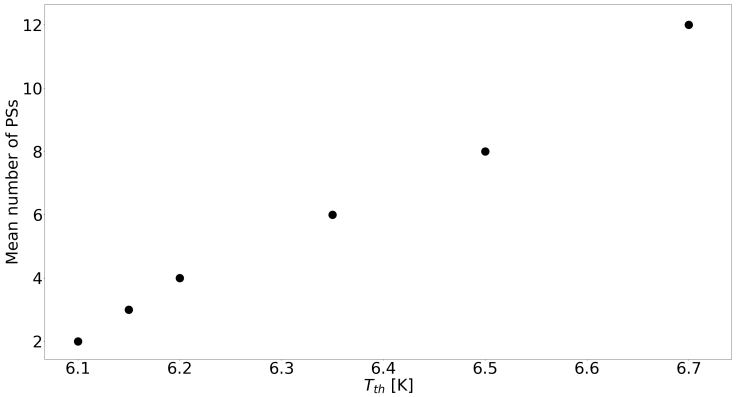

Figure 2.9: The mean number of PSs necessary to simulate distributions in Figure 2.8.

The position of the distributions can be modulated also varying the critical current I_c, as shown in Figure 2.10.

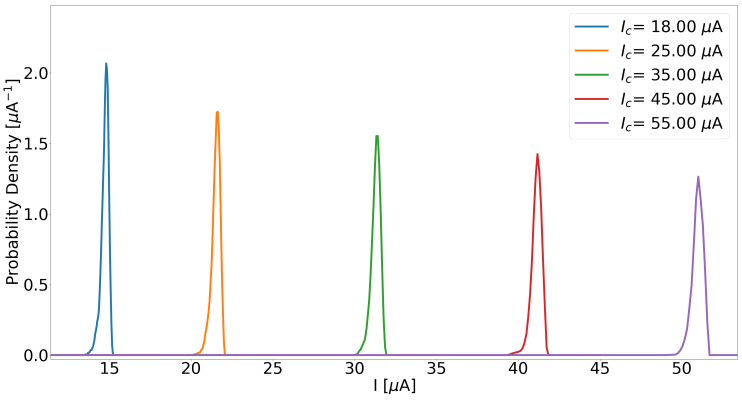

Figure 2.10: Simulated SCDs with different critical current values are presented. These simulations are done at $T = 0.9\,\mathrm{K}$ with $T_{th} = 1.07\,\mathrm{K}$.

In Figure 2.10 different distributions are calculated for different values of I_c, fixing T and T_{th}. The SCDs in Figure 2.10 show that $\langle I_{sw} \rangle$ increases with the increasing I_c. Keeping in mind what has been said in Section 1.6.1, I_c values defines the energy scale of the phenomenon. Indeed, as I_c increases, the free-energy barrier becomes higher, according to Equation (1.49). As I_c increases, simulated SCDs have a larger σ, as predicted in Equation (2.2) and can be noted from the peak height of the distributions with normalised area in Figure 2.10.

Chapter 3

Experimental Setup

In this work, two cryogenic systems have been used to study the transport properties of different nanostructures: the *Heliox* ^{3}*He* system and the *Triton* dilution fridge. The samples fall in two classes: Al nanowires and three *nanomeanders*, i.e. meandered nanostrips, made of NbTiN and NbN. For all these samples, transport measurements have been done, in particoular measurements of current-voltage I-V characteristics and switching current distributions. The Heliox ^{3}He system can reach the base temperature of 300 mK and has been used to collect data between the base temperature and the critical temperature of the nanomeander devices, of the order of 10 K. Nanodevices with different geometries may have a direct application as single photon detectors with possible impact also in the field of quantum technologies, therefore thier trasport properties have been studied at very low temperatures by using the Triton system, which reaches a base temperature about 10mK. For both cryostats, the filtering system will be described. The electronic setup is the same for both cryostats and will be illustrated in the last part of this chapter.

3.1 Samples

In this work, meandered nanostrips made of NbN and NbTiN have been studied, also by virtue of their application as superconducting nanowire single-photon detector (SNSPD) [32]. These two materials have similar growth condition and bulk T_c and, furthermore, their high detection efficiency is well known [26, 47, 48].

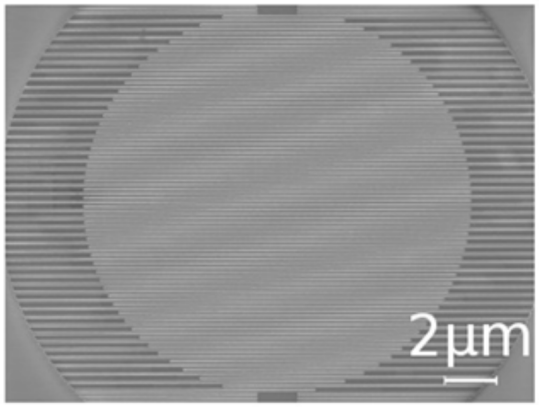

Figure 3.1: NbTiN nanomeander: the darker lines represent the superconducting material, while the brighter ones represent the substrate [32].

To realise these nanostructures, a substrate of thermally oxidized Si, polished with acetone, has been covered with a NbTiN (NbN) thin film deposited by reactive DC-magnetron sputtering in an Ar + N_2 gas mixture. On the superconducting material, PMMA (*polymethylmethacrylate*) has been deposited through spin-coating. The PMMA is a resist material, i.e. an electrosensitive material. To let evaporate the solvent in the resist, the chip is put in a fan oven at 180 °C for a minute. Thus, the resist is exposed to electric beam lithography (EBL), during which a part of the resist is covered with a negative mask of the final device. In this way, the resist structure has the same geometry of the final device. Now, the sample can be exposed to ion beam etching (IBE) with Ar^+. Indeed the resist is not sensitive to the argon ions and only the NbTiN (NbN) exposed is etched. Finally, the chip is immersed in acetone to remove the remaining resist.
Therefore, the NbTiN (NbN) is nanostructured in meandered strips 80 nm wide and 5 nm (7 nm) thick [32]. It is important to recall that the nanomeander is composed by strips, not wires: actually the coherence length of NbTiN (NbN) is $\xi = 4.5\,\text{nm}$ ($\xi = 6\,\text{nm}$) [49, 50], which is smaller than the width and comparable with the thickness. Moreover, the length of the meander is $L = 0.8\,\text{mm}$. The T_c values of these samples are almost the same. The whole nanostructure is confined to a circumference with a diameter of 15 μm, where the strips are spaced of 90 nm, as shown in Figure 3.1. This geometry has been choosen to increase the active region of the detector: a photon can impact on more sections of the same nanowire. A detailed analysis of the fabrication process can be found in Ref. [26].

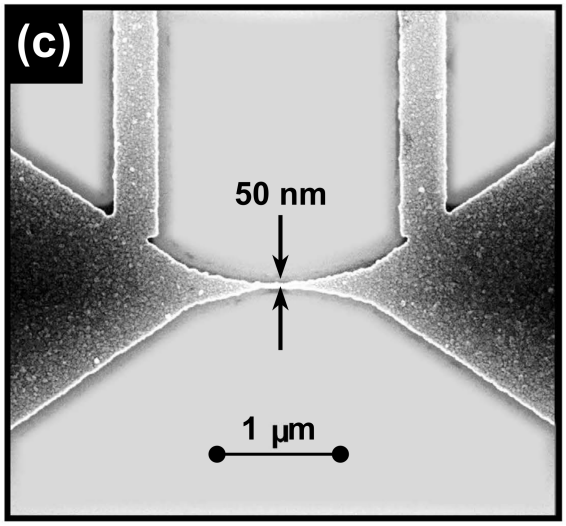

Figure 3.2: Scanning electron microscopy image of an Al nanowire [29].

As a term of comparison, superconducting Al nanowires have been measured down to 300 mK. These devices have been realised in Liège [29], depositing Al on Si/SiO_2 substrates by using molecular beam epitaxy (MBE). The geometry is realised by following a process similar to the one described above. The nanowire has a length of 1.5 μm, with a thickness $d \sim 25$ nm and a width $w = 50$ nm. Since the Al coherence length is 120 nm, these samples can be considered 1D-superconducting devices [29].

3.2 Heliox

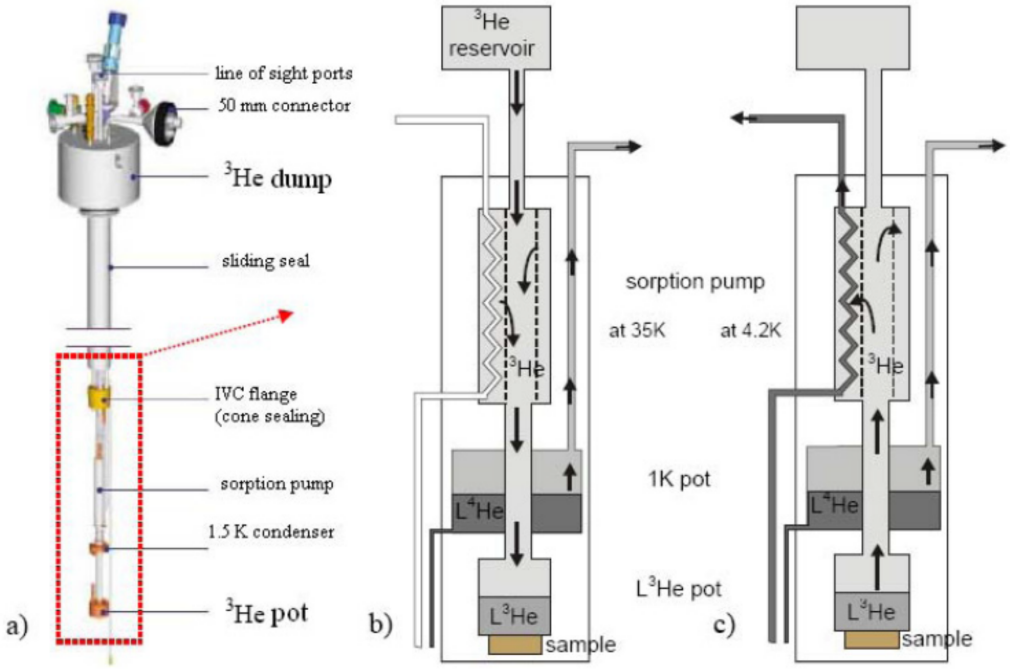

Figure 3.3: In (a) the Heliox system is described. In (b) the ^{3}He condensation process is reported. In (c) the activation of the sorption pump to achieve the base temperature is shown.

The Heliox ^{3}He is an evaporation cryostat, i.e. a cryogenic system capable to reach low temperatures due to the reduction of the vapour pressure of liquid ^{3}He. The system structure is shown in Figure 3.3. The fridge is formed by a sorption pump, a 1 K-pot and an ^{3}He-pot and the whole fridge is isolated from the external environment by a brass cylinder, the inner vacuum chamber (IVC). In the IVC, vacuum is created by an external rotary pump, in order to decouple the fridge from the ^{4}He bath. The fridge is dipped in a liquid ^{4}He bath and a small amount of ^{4}He gas is inserted as exchange gas between the bath and the fridge: if the gas amount is too much, the system is not able to go below 4.2 K. Once the liquid helium temperature is reached (about 4 K), the 1 K-pot is filled with liquid ^{4}He from the bath, by using a cannula that goes outside the IVC, as shown in Figure 3.3b. Thanks to a rotary pump connected to the 1 K-pot, the vapour pression can be decreased, using a needle valve to control the vapour pression inside the chamber. When the pression is about 1mbar, the 1 K-pot goes under 2 K, so the ^{3}He starts to condense in the ^{3}He-pot. At the same time, the sorption pump temperature is

kept over 35 K. This is made necessary because the sorption pump is a cilinder of a zeolitic material able to absorb ^{3}He molecules: above 35 K the sorption pump is not active, then it starts to pump ^{3}He molecules when cooled down to a few Kelvin. Therefore, when the condensation of ^{3}He in the ^{3}He-pot is terminated, the sorption pump heater is turned off, in order to decrease the vapour pressure in the ^{3}He-pot and a base temperature of about 300 mK is reached. As it can be seen in Fig. 3.4, the vapour pression of ^{3}He is about 10^{-3} mbar.

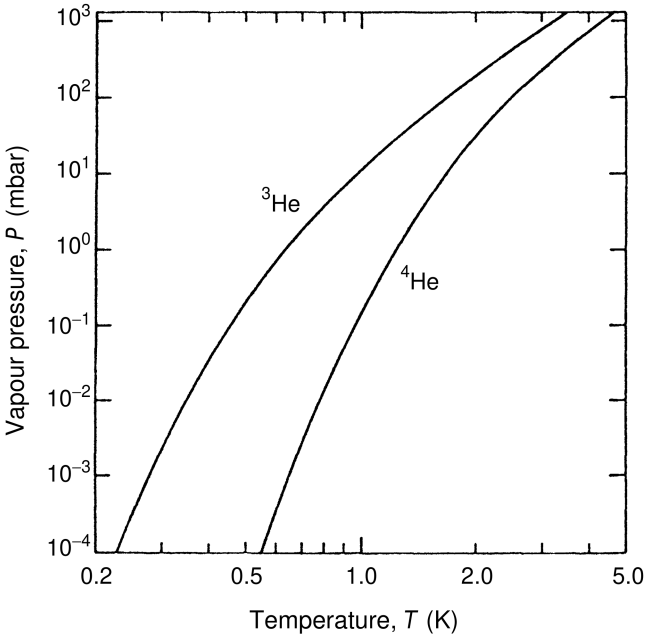

Figure 3.4: ^{3}He and ^{4}He phase diagrams *(P,T)* [51].

The sample is glued on a copper holder attached to the ^{3}He-pot, to which it is thermically anchored. Thanks to the heaters on the sorption pump and on the ^{3}He-pot, the system is able to thermalise at any temperature between $0.3 \div 100$ K. To avoid the sample heating due to the current flow, different kinds of wire are used in the fridge. From room temperature down to the sample stage, manganin (86% of Cu, 12% of Mn and 2% of Ni) wires are choosen for voltage lines, due to their thermal conductivity that at low temperatures is about two orders of magnitude smaller than copper's one. On the other hand, manganin has higher resistivity, therefore copper wires are used for current lines down to the 1 K-pot. Then, to ensure that high currents wouldn't effect the thermal stability, from the 1 K-pot to the sample stage, current wires made of a superconducting alloy of Nb and Ti ($T_c \approx 11$ K) are employed. The sample is bonded with Al wires on a chip with golden pads, which are electrically connected to the cryostat lines, once the chip

is attached to the ^{3}He-pot stage.

3.3 Triton

The Triton system is a "dry" dilution fridge, where dry stands for cryogenic liquid free. Indeed, this system doesn't need any external source of liquid helium: it is possible to reach the base temperature (about 10 mK) thanks to a pumping system acting on a mixture of ^{3}He-^{4}He. As it can be seen in in Fig. 3.5, depending on ^{3}He concentration x

$$x = \frac{n_{^3He}}{n_{^3He} + n_{^4He}}$$

it is possible to find a range of temperature where there is a coexistence of two phases: a lighter diluted one floating on a saturated one. The diluted phase is composed mostly of ^{4}He with about 6% of ^{3}He in it, instead the saturated one is composed almost completely of ^{3}He.

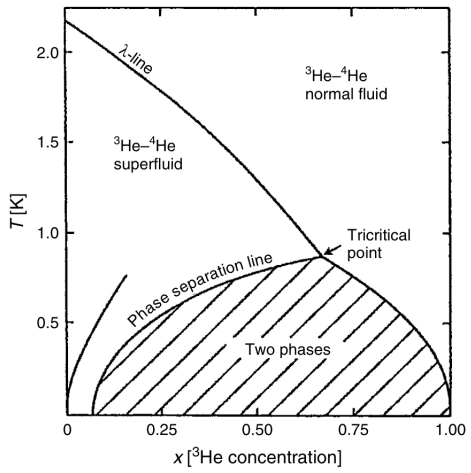

Figure 3.5: Phase diagram of a ^{3}He-^{4}He mixture [51].

The Triton system is essentially described in Figure 3.6, where the principal components of the condensing line are indicated.

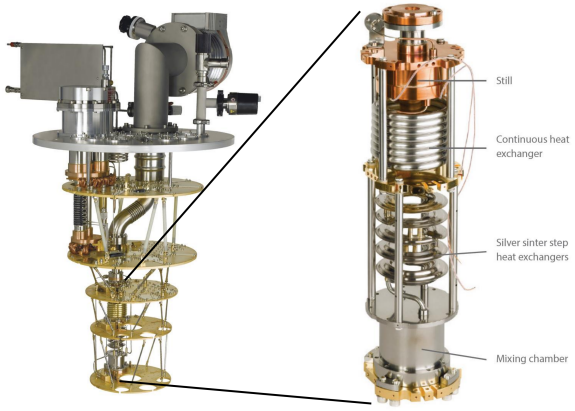

Figure 3.6: Triton system description.

To isolate the cryostat, an IVC is present and the vacuum is created in it with an external pump. In Figure 3.6 it can be seen the presence of a *still*, several *heat exchanger* and a mixing chamber. The mixing chamber is where the two phases of the ^{3}He-^{4}He mixture coexist and it is connected to the still. The still is a stage where ^{3}He is "distilled" from the mixing chamber and flow to the pumping lines. If the temperature has a quick drop, the vapour pressure would be so low that circulation stops. For this reason, the still has a heater to control the temperature decrease. As much as it is given power to the still, the circulation rate will be higher, which means more cooling power. Otherwise, too much power to the still heater leads to an increase of ^{4}He vapour pressure that decreases the dilution efficiency: therefore the optimal still temperature is $0.7 \div 0.8\,\mathrm{K}$.
It can be noticed that there is no 1 K-pot, which has been replaced with by a heater exchanger in the still pumping line. The heater exchanger and the Joule-Thompson expansion make possible to condense the ^{3}He gas. In the first cooling steps, the pressure of Joule-Thompson expansion is $\sim$ 2.5 bar, but near the base temperature it drops to $\sim$ 0.5 bar: indeed the need to reach high pressure makes it necessary the presence of a compressor.
As in the Heliox system, even in the Triton we have different materials for voltage and current lines. The first ones run from the fridge's head with constantan (55% of Cu and 45% of Ni) wires, until they reach the first filtering stage at about 4 K. There manganin wires are used for voltage lines down to the sample holder located under the mixing chamber. The material choice is made to reduce as much as possible the system heating. For the same reason, current lines are made of copper until the first filtering stage at 4 K, then NbTi superconducting wires are used to reach the sample stage.

3.4 Filtering system and electronic setup

In order to perform low temperature measurements of the transport properties of superconducting devices, an accurate filtering system is required to reduce thermal and electromagnetic noise. Concerning thermal noise, different materials for voltage and current lines, as described in the previous Section, are suitable to ensure progressive and optimal thermalization of the measurement lines. On the other hand, to reduce the electromagnetic noise, two stages of filters for both voltage and current lines are used. The first stage of filtering is a low-pass RC-circuit, which is used on both Triton and Heliox systems. These RC-filters have a typical cut-off frequency of about 1 MHz and are located at the 1 K-pot stage in the Heliox. In the Triton, the filters are located at 4 K-plate, i. e. above the still plate. These filters lose in attenuation at higher frequencies, especially above a few GHz, thus another filtering stage is needed to reduce the electromagnetic noise in the GHz range. This stage of filtering is composed by copper-powder (CP) filters, which have a cut-off frequency in the range of few GHz. In the Heliox there are two CP filters, placed at the 1 K-pot and at ^{3}He-pot. Instead, in the Triton CP filters are situated at the 100 mK stage (the cold plate, a stage between still and mixing chamber).
The electronic setup is the same for both the cryogenic systems. A list of the measurements instruments is described below:

- *LeCroy Wave Runner 6100A* oscilloscope;
- *SR570 Stanford Research Systems* preamplifier;
- *Agilent 33120A* waveform generator;
- *EG & G Princeton Applied Research 5210* lock-in amplifier.

The transport measurements are performed by using a 4-point contact technique, where two contacts are used for current bias of the nanostructure and two contacts are used to read the voltage drop across the device. This measuring technique is used to exclude the voltage drop due to the filter impedance. The two voltage lines V_- and V_+ are sent to a differential amplifier, with variable gain between 10 and 500 and the output is measured on the oscilloscope.
In Figure 3.7 the measurement setup is shown.

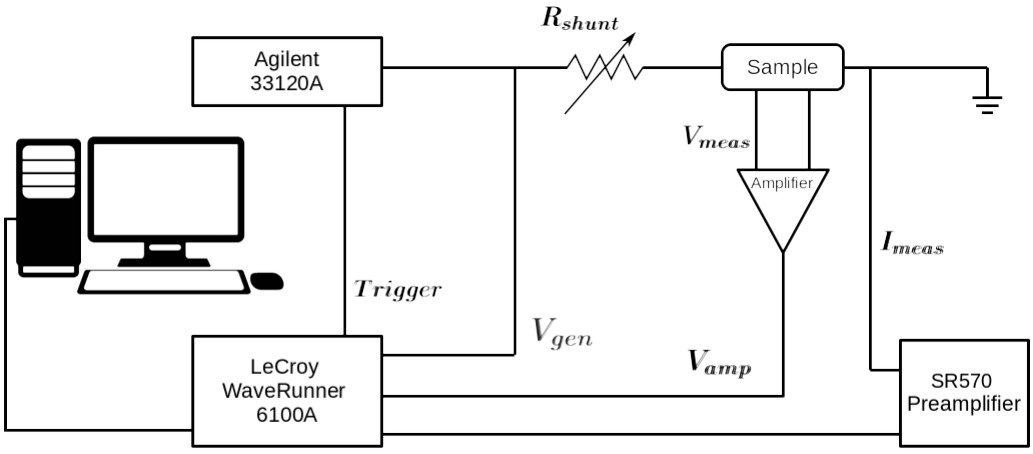

Figure 3.7: Measurement setup that has been used in this thesis.

A triangular waveform is generated by *Agilent 33120A*, at low frequency in the order of $10 \div 20$ Hz and with a peak-to-peak amplitude V_{pp}. To current drive the nanostructure, the voltage V_{pp} is sent on a shunt resistance R_S, so that the bias current across the sample is

$$I_{bias} = \frac{V_{pp}}{R_S + R_N} \tag{3.1}$$

where R_N is the sample resistance. Since $R_N << R_S$, it can be neglected. The current passing through the nanomeander is preamplified in the *SR570 Stanford Research Systems* and then measured on the oscilloscope.
By using the same setup, it can be acquired both the I-V characteristics and the switching current distributions. In the first case, an average over 100 sweeps is made to further reduce the electromagnetic noise. To measure the switching current distributions, a threshold voltage V_{th} is set on the oscilloscope: if the voltage drop across the nanostructure overcome V_{th}, the corresponding bias current is recorded. After a sufficiently high number of switching events, of the order of 5000, the resulting switching current distribution is exported. The oscilloscope is connected to a computer, where all the data are recorded.
In the two cryogenic systems, there are of three kind of resistance thermometers: *Cernox, RuOx* and *Pt100*. The first ones are resistance thermometers made of ceramic zirconium oxynitride, with a temperature range from room temperature to 1.5 K. The RuOx (RUthenium OXide) thermometers are thick-film resistors that work only at low temperature, i.e. from 10 mK to 40 K. The last ones are platinum

resistance thermometers that work in the range from 30 K to 873 K [52]. For standard operation in the Triton system, two are the places where it's fundamental to control the temperature: the still plate, that has a RuOx thermometer, and the mixing chamber, that has a RuOx and a Cernox thermometer, in order to cover the full temperature range from room temperature down to the base temperature of about 10 mK. Anyway, every plate of the system has at least one thermometer, in case of more specific applications, which are outside the goals of this thesis.

3.4.1 Measurements errors

The filtering scheme described in the previous Section allows to perform low noise measurements. Maximum errors can be estimated from the *I*-*V* characteristics, as shown in Figure 3.8. In the inset of the figure, a zoom of the superconducting branch highlights the corresponding noise figure.

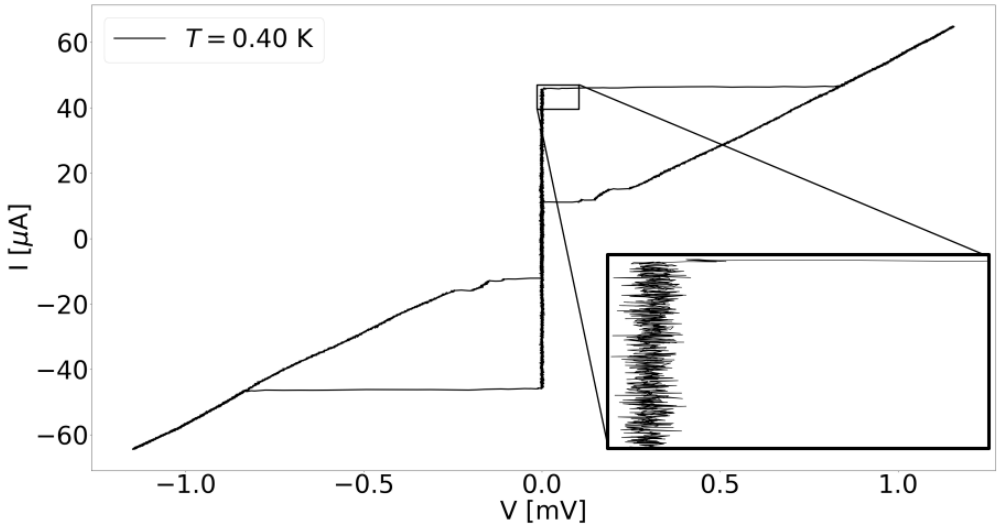

Figure 3.8: The fluctuations in the *I*-*V* characteristic can be used to determine the maximum error of a measurement. The presented *I*-*V* characteristic refers to an Al nanowire at $T = 0.4$ K.

The maximum errors can be estimated as half of the noise figure measured on the IV characteristic. Since the nanostructures are current biased, the errors on the current values are smaller than the errors on the voltage drop across the device. The percentage errors on the voltage values are about 1% and have been determined as the ratio between the noise amplitude and the maximum voltage value measured on the *I*-*V* characteristic. The same approach has been used to determine the errors on the current values, leading to percentage errors of the

order of 0.5%. These errors propagate on the estimate of other quantities, such as the normal resistance R_N, for instance.
The errors on the mean switching current $\langle I_{sw} \rangle$ and of the standard deviation σ can be estimated by considering the following relation [53]:

$$\delta f = \sqrt{\sum_i \left(\frac{\partial f}{\partial x_i} \delta x_i \right)^2}$$

where f is a function of the quantities x_i affected by an error δx_i. Since a switching event is recorded when the voltage overcomes a threshold value, the error on the switching event depends on the voltage error. As it is well known, in experiments where stochastic events are counted, the uncertainty on the number of events collected in a specific bin is equal to the square root of the counted events, i.e. $\delta n_k = \sqrt{n_k}$, where n_k is the number of switching events at I_k [53]. Since the error that affects the current measurements is significantly smaller than the voltage error, δI_k can be neglected in the propagation of errors:

$$\delta I_{mean} = \frac{\sqrt{\sum_k (I_k \delta n_k)^2}}{N} \qquad \delta\sigma = \frac{\sqrt{\sum_k ((I_k - I_{mean})^2 \frac{\delta n_k}{N})^2}}{2\sigma}$$

where $\sum_k n_k = N$. The errors estimated in this way are about $1\% \div 2\%$ of the measured values of the mean switching current $\langle I_{sw} \rangle$ and on the standard deviation σ.
Concerning T_c, its values are estimated from the I-V characteristics, as the temperature at which the superconducting branch disappears. Thus, its error can be estimated as the half of the difference between the temperature of the first I-V curve which does not show any supercurrent and the last temperature at which the superconducting branch appears.

Chapter 4

Experimental results

In this chapter, the I-V measured on different nanowires and nanomeanders characteristics are shown. Experimental switching current distributions (SCDs) are then presented and analysed by using the model presented in Chapter 2.
Since the nanomeanders are great candidates for superconducting nanowire single-photon detectors (SNSPD), the standard deviation behaviours are analysed to identify the dissipation mechanisms and therefore the best temperature range of application.

4.1 *I-V* as a function of the temperature T

Due to the their geometrical structure, the samples fall in two different regimes of Likharev's diagram, as discussed in Section 1.5. Differences between the presentend nanostructures and Josephson junctions are evident from the analysis of the I-V characteristics, as partly discussed below and as widely acknowledged in literature [29–31, 33, 34, 54].

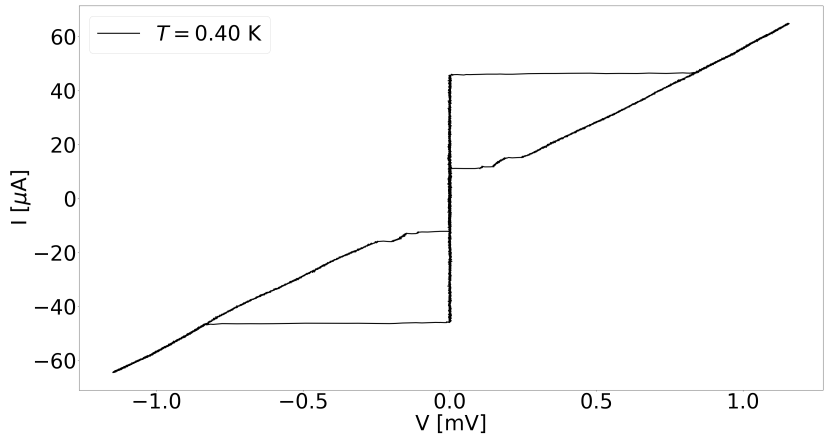

Figure 4.1: *I-V* characteristic of the Al nanowire at the bath temperature $T_b = 0.4\,\mathrm{K}$.

In the *I-V* characteristic of an Al nanowire at $T_b = 0.4\,\mathrm{K}$ (Figure 4.1), the superconducting, the normal and the retrapping branches can be easily identified with the criteria, which have been summarized in Section 2.1. Once the switching current is exceeded, there is a voltage jump to the resistive branch, which is commonly:

$$V_{sw} = I_{sw} R_N$$

where I_{sw} is the switching current and R_N is the normal resistance, which can be estimated from the normal branch slope. In Josephson junctions the switching voltage is proportional to the sum of the two superconducting gaps, i.e. $V_{sw} = |\Delta_L + \Delta_R|/e$ [23], where the subscript symbols are referred to the left and right superconductor, respectively. In the Al nanowire, the normal resistance has been found to be $R_N = 16.74 \pm 0.2\,\Omega$ and the switching current $I_{sw} = 45.97 \pm 0.4\,\mu\mathrm{A}$, thus the $V_{sw} = 0.82 \pm 0.02\,\mathrm{mV}$ is estimated applying the previous equation and is consistent with the measured value on the *I-V* characteristic shown in Figure 4.1. The errors have been estimated following the considerations done in Section 3.4.1. Since the energy $eV_{sw} = 0.82 \pm 0.02\,\mathrm{meV}$ is almost twice the superconducting gap of the Al, which is $2\Delta_{Al} = 0.4\,\mathrm{meV}$, the voltage jumps are consistent with the typical behavior of Al nanowires [30]. This is a further confirm that these Al nanowires cannot be considered in the Josephson regime, according to Likharev's criterion (Section 1.5). These considerations are done on the *I-V* characteristics, since the study of the switching current fluctuations is the main topic of the analysis pursued in this thesis. Indeed, substantial differences would be immediately evident from the *I-V* characteristics as a function of the applied magnetic field.

The *I-V* characteristics have been measured at different temperatures and are presented in Figure 4.2.

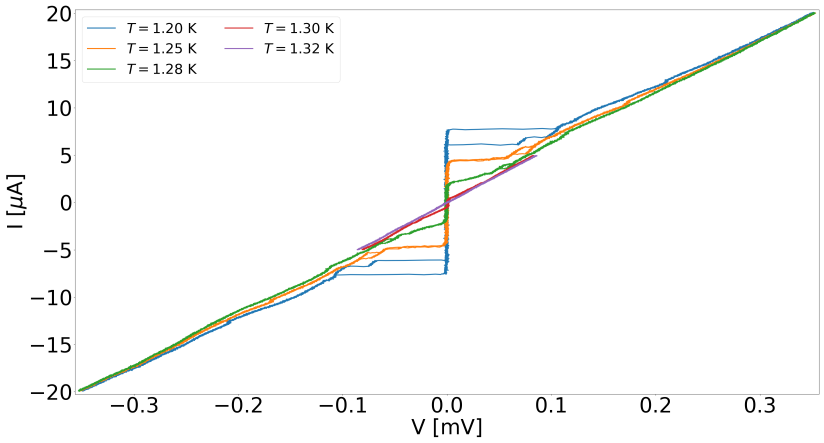

Figure 4.2: *I-V* characteristics at different temperatures of Al sample. At $T = 1.32\,\mathrm{K}$ the superconducting branch disappears.

The superconducting branch disappears between $T = 1.30\,\mathrm{K}$ and $T = 1.32\,\mathrm{K}$, where the *I-V* is completely linear up to $V = 0.08 \pm 0.01\,\mathrm{mV}$. Thus, $T_c = 1.31\,\mathrm{K}$ will be considered as the critical temperature of the Al sample. As the temperature decreases, the critical current I_c obviously increases.
The *I-V* characteristics are strongly different in nanomeanders, which nominally fall in the Abrikosov vortex motion zone of the Likharev's diagram (see Figure 1.11).

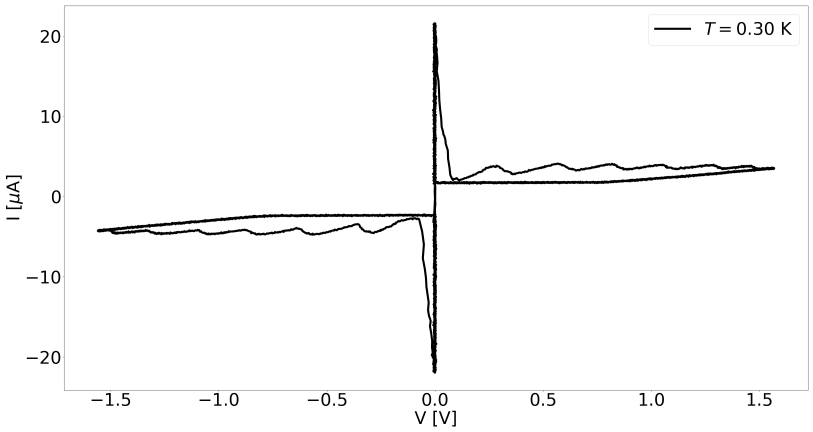

Figure 4.3: *I-V* characteristic of the NbTiN nanomeander at $T = 0.3\,\mathrm{K}$.

Differently from the Al samples, there is no sharp jump to a finite voltage, but a jump with a current suppression, as reported elsewhere in literature (see for instance Refs. [25, 32]). This behaviour is due to the normal resistance of the nanomeander, which is larger than the shunt resistance. The nanostructure is current driven until the switching current is reached. In the resistive branch, there is a jump in the bias current, according to:

$$I_{bias} = \frac{V_{pp}}{R_S + R_N}\,.$$

Measuring the bias current and the voltage in the increasing linear segments of the normal branch, it is possible to estimate the normal resistance $R_N = 250 \pm 50\,\mathrm{k}\Omega$ applying the previos equation.
The critical temperature can be found from the *I-V* characteristics at different temperatures, which are reported in Figure 4.4a and in Figure 4.4b.

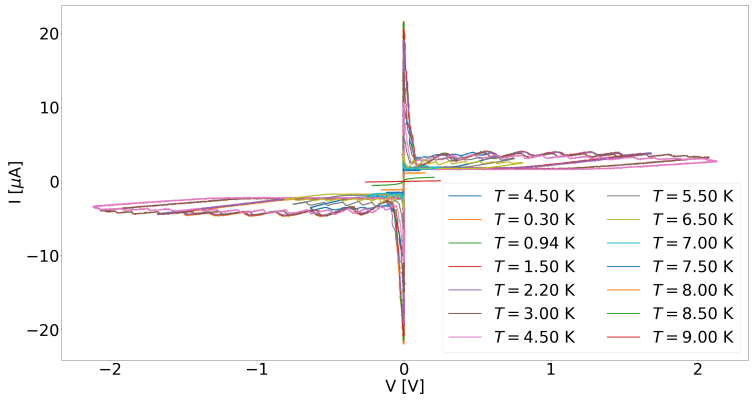

(a)

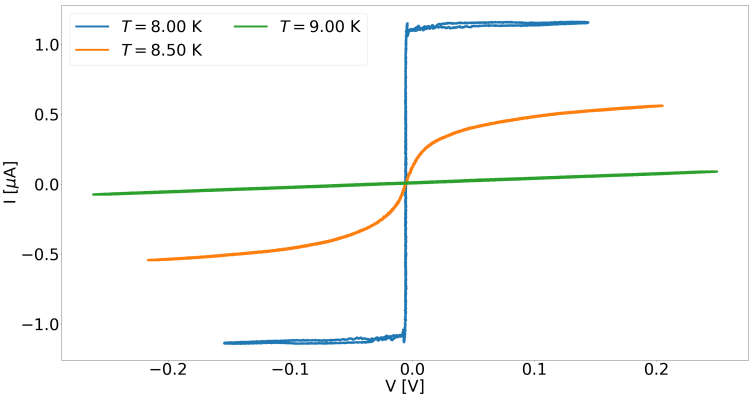

(b)

Figure 4.4: a) *I-V* characteristics measured at different temperatures for the NbTiN nanomeander. b) Zoom of the *I-V* characteristics near T_c.

In Figure 4.4b, it can be noticed that the superconducting branch disappears between $T = 8.5\,\mathrm{K}$ and $T = 9\,\mathrm{K}$, hence the nominal value $T_c = 8.5\,\mathrm{K}$ is considered as the critical temperature of the NbTiN sample. In analogy to the Al nanowire, also for both nanomeanders the relation among the switching voltage and the superconducting gaps does not hold. Indeed, the voltage jumps are $\sim 100\,\mathrm{meV}$ and, for example, the superconducting gap of NbTiN is $1.3\,\mathrm{meV}$. The same considerations can be done for the NbN nanomeander, whose *I-V* characteristic at $T = 0.3\,\mathrm{K}$ is shown in Figure 4.5.

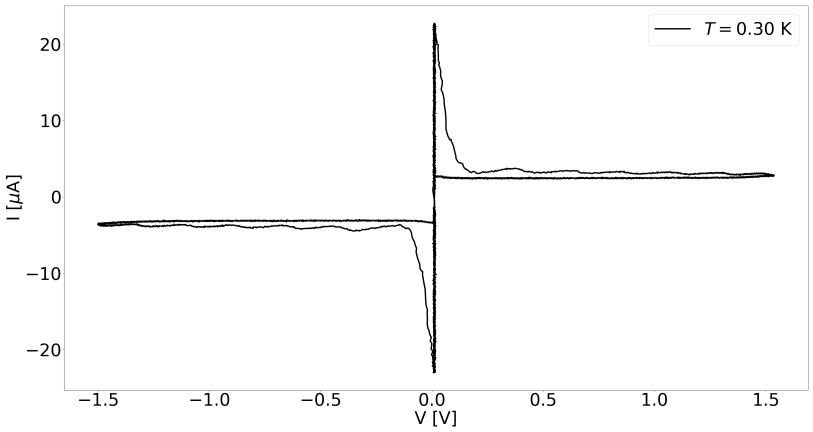

Figure 4.5: I-V characterstic of the NbN nanomeander at $T = 0.3\,\mathrm{K}$.

As for the NbTiN sample, the normal resistance $R_N = 360 \pm 50\,\mathrm{k\Omega}$ is comparable with the shunt resistance, giving an I-V characteristic similar to the NbTiN ones. A critical temperature $T = 8\,\mathrm{K}$ has been found.
All the characteristic parameters of the samples are summarised in the following table, where J_{sw} is the nominal current density, D is the thickness, W the width, L is the length and $\xi(0)$ is the coherence length.

Sample	T_c (K)	R_N (Ω)	J_{sw} (MA/cm^2)	D (nm)	W (nm)	L (μm)	$\xi(0)$ nm
Al	1.31	16.7 ± 0.2	3.80	25	50	1.5	120 [29]
NbTiN	8.5	$(250 \pm 50) \cdot 10^3$	5.49	5	80	800	4.5 [49]
NbN	8	$(360 \pm 50) \cdot 10^3$	4.15	7	80	800	6 [48]

4.2 Experimental SCD

SCDs have been collected acquiring 5000 switching events at different temperatures, as specified for each sample in the relative caption. Concerning the Al nanowire, the distributions have been measured in the temperature range of $0.3 \div 0.9\,\mathrm{K}$ and are shown in Figure 4.6.

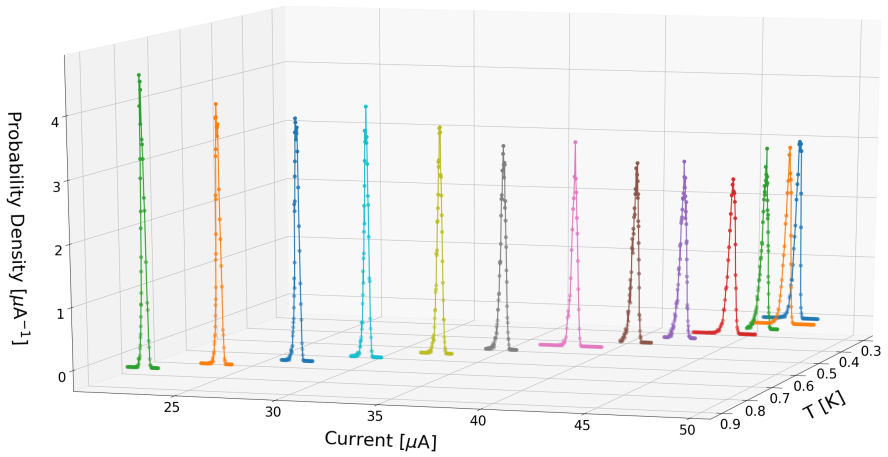

Figure 4.6: SCDs for the Al nanowire measured between 0.3 K and 0.9 K.

The mean switching current values vary in a wide range between $\langle I_{sw} \rangle = 47.5 \pm 0.7\,\mu$A, at $T = 0.35$ K, and its minimum $\langle I_{sw} \rangle = 22.8 \pm 0.3\,\mu$A, at $T = 0.9$ K. The errors have been estimated by using the arguments reported in Section 3.4.1.
All the SCDs show a left tail longer than the right one, i.e. a negative skewness [25, 32, 55]. As described in Section 2.2, the Kurkijärvi theory gives prediction on the statistical momenta in the single event regime that is the temperature range in which a single thermally activated process can induce the transistion from the superconducting to the resistive state. According to Equation (2.2), the σ should be proportional to the temperature and for this reason it should increase with T. In Figure 4.7, the σ of the Al sample is shown as function of the temperature.

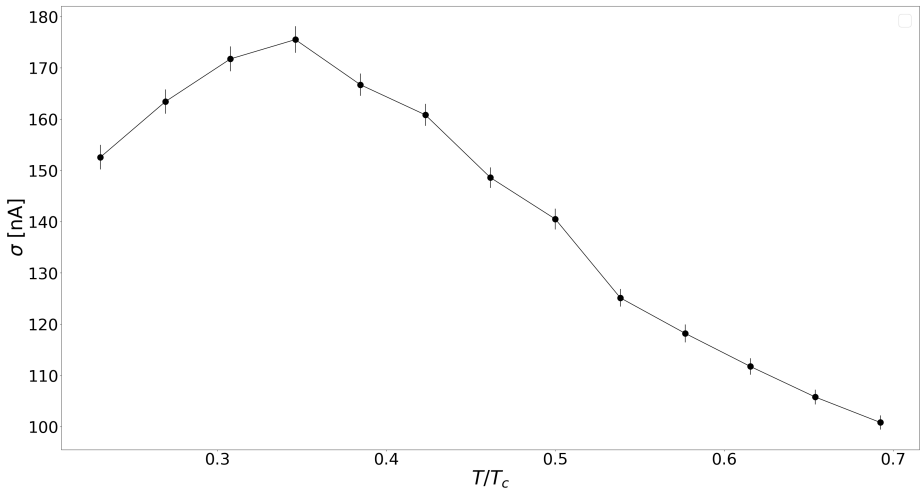

Figure 4.7: $\sigma(T)$ of the SCDs measured on the Al nanowire.

Following the considerations developed in Section 2.2, this behaviour induces to recognise the single event region in the increasing σ regime, in analogy to Refs. [25, 29, 32]. The decreasing σ regime is not expected considering only thermal activation processes, hence more sophisticated considerations will be done in Section 4.3 in order to describe this counter-intuitive behavior.
For the nanomeanders, the SCDs have been measured for temperatures between 0.3 K and 6 K. In Figure 4.8, NbTiN SCDs are presented.

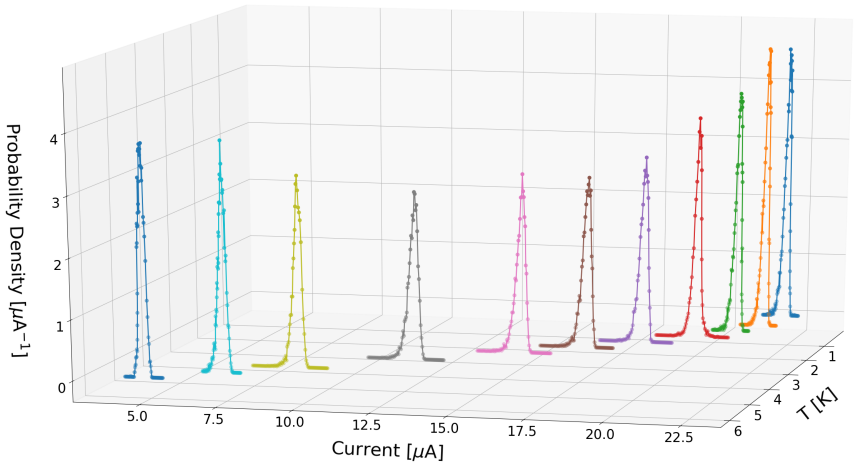

Figure 4.8: SCDs for the NbTiN nanomeander measured between 0.3 K and 6 K with a mean switching current that varies between 4.76±0.06 μA and 22.0±0.3 μA.

For both nanomeanders, the mean switching current values are monotonically decreasing as the temperature approaches T_c. In Figure 4.9 the behaviours of normalised I_{mean}/I_c are shown as a function of the normalised temperature T/T_c, where I_c is the maximum mean switching current of each sample measured at the lowest temperature $T = 0.3\,\mathrm{K}$.

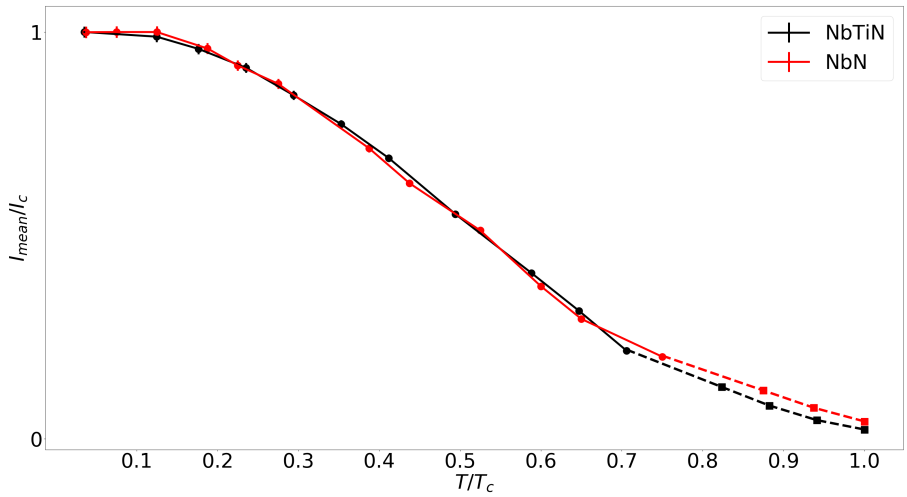

Figure 4.9: The behaviours of normalised I_{mean}/I_c as a function of the normalised temperature T/T_c for NbTiN and NbN nanomeanders are shown. The square points above $0.7\,T_c$ are the values estimated from the I-V characteristics. The error bars are within the experimental point dimensions.

The two behaviours are very similar thus suggesting the same type of dissipation mechanisms, as discussed Section 1.4. The similarities between the two samples can be also seen from Figures 4.10a and 4.10b.

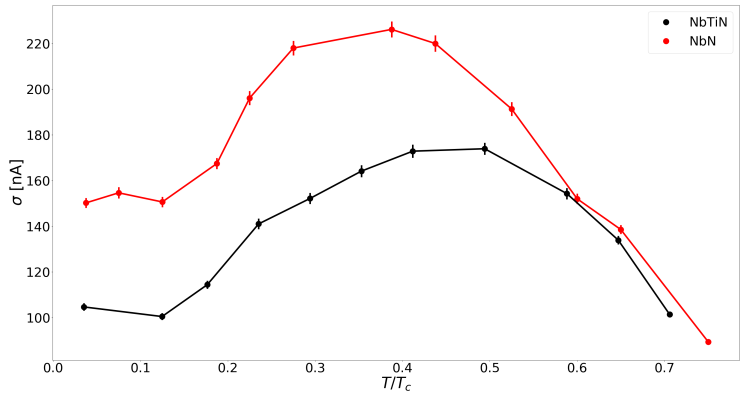

(a)

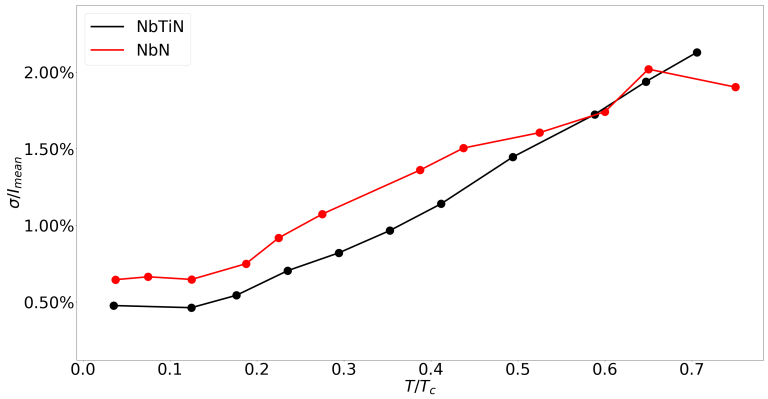

(b)

Figure 4.10: In (a) the standard deviation behaviours for both nanomeanders are presented as a function of T. In (b) the ratio between the standard deviation and the mean value of the switching currents for both nanomeanders are presented as a function of T. The error bars are within the experimental point dimensions.

Both samples show the same σ behaviour: the standard deviation increases until $T = 0.4\,T_c$ and then it decreases. Whereas the first region can be easily described in the framework of Kurkijärvi theory, the decreasing region needs a more sophisticated analysis (see Sections 2.3 and 4.3).
Other similarities can be seen from the behaviour of σ/I_{mean}, which is always increasing, except at very low temperatures, where the ratio saturates. In this region, σ has a temperature-indipendent behavior, with different values for each sample, as it can be seen in Figure 4.10a. This behaviour will be later discussed

in Section 4.3.
Since the increasing σ region could be identified as the single event region [25, 29, 32,37,39], the temperature ranges of these regimes are listed in the following table.

Sample	ΔT (K)
Al	$0.3 \div 0.45$
NbTiN	$0.3 \div 4.2$
NbN	$0.3 \div 3.1$

4.3 Fitting of experimental curves and discussion of physical parameters

The σ values presented in the previous section are not always increasing as a function of the temperature, as it should be if only stochastic heating events would take place during the current flow. At higher temperatures, σ decreases and the best fit curves according to Kurkijärvi theory [40] would require non-physical parameters to fit the experimental data. These fits have been obtained on the $P(I)$ curves, as shown in Figure 4.11, following the approach described in Section 2.2.1 and Equation (2.14). The simulated $P(I)$ curves have been obtained by considering the escape rate Γ based on thermally activated phase slips, as defined in Equation (1.48). This is the standard fitting procedure used also on junctions [23,30,56]. In Figure 4.11, solid lines are the best fit curves for the NbTiN nanomeander.

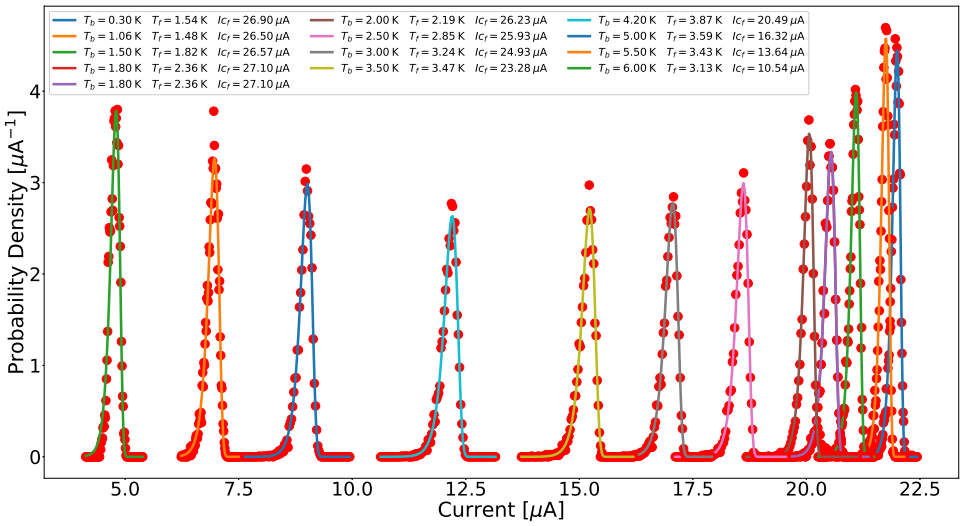

Figure 4.11: Experimental SCDs at different temperature for the NbTiN nanomeander. Solid lines are the best fit obtained using the TAPS model.

For the NbTiN, since for a bath temperature larger than 4.2 K the fitting temperature T_f is significantly lower than T_b and since there is no way the system could cool down in presence of a current flow, T_f values obtained by the fit are considered not reasonable. For all the samples, the fitting temperature is non-physical in the temperature range where the standard deviation σ presents a decreasing behavior as a function of the T.

T_b (K)	T_f (K)
5	3.59
5.5	3.43
6	3.13

This is a direct proof that the standard fitting procedure does not work for these samples. It is necessary to go beyond and to study the systems in terms of heating diffusion, as reported in Refs. [29, 42, 55] and to use the model presented in Section 2.3. The following results are in accordance with Ref [29] and there is a robust self-consistency between the physical parameters of all samples investigated in this work as a function of temperature. In this analysis, the switching events are assumed to be caused by thermally activated phase slips, according to the LAMH model presented in Section 1.6.1, and heat dissipation is regulated by the arguments reported in Section 2.3. All the fitting curves presented in this section are done with $N = 4000$ stochastic events, obtained by varying I_c, T_{th} and T_{eff}, whose

physical meaning and influence on the $P(I)$ have been discussed in Section 2.4. For all the samples, the threshold temperatures T_{th} as such that $0.11\,\mathrm{K} \leq T_{th} - T \leq 0.20\,\mathrm{K}$, in accordance with Ref. [29]. Indeed, threshold temperatures have been choosen keeping in mind that in the decreasing region of σ behaviours as a function of the temperature T should be fitted with multiple phase slips. For all the samples, the mean number of phase slips behaviours as a function of the temperature T is increasing proportionally to T.
Moreover, to fit the experimental SCDs, the critical currents have been choosen expecting a decreasing behaviour as a function of the temperature T for each sample, according to Refs. [29,30,37]. The critical current behaviours as a function of th temperature T for each sample can be seen in Figure 4.12.

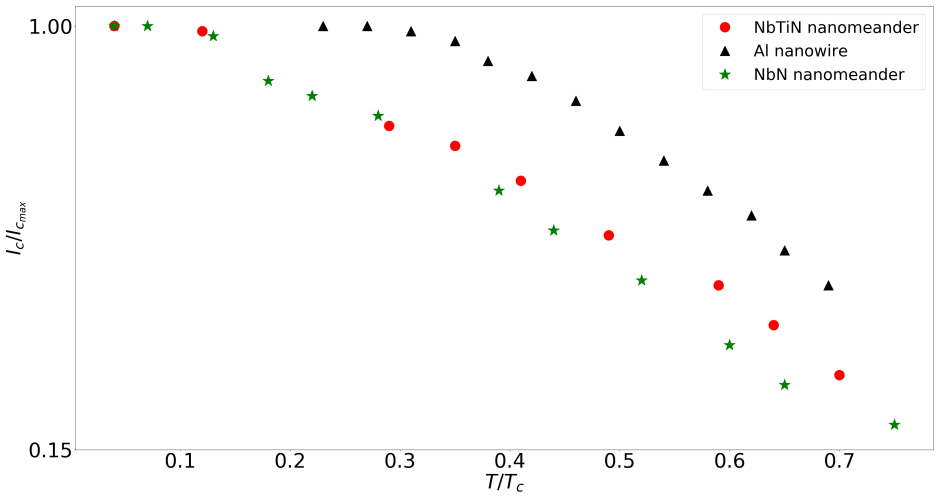

Figure 4.12: Critical currents used in simulations normalised to their maximum value as a function of the normalised temperature.

The parameters used to fit the experimental SCDs of the Al nanowires are self-consistent and in remarkable accordance with the experimental conditions and results, as reported in Ref. [29]. In Figure 4.13, the fitting curves are the solid lines superimposed on the measured SCDs for the Al nanowire. To obtain these curves, the bath temperature has been used as the effective temperature T_{eff}.

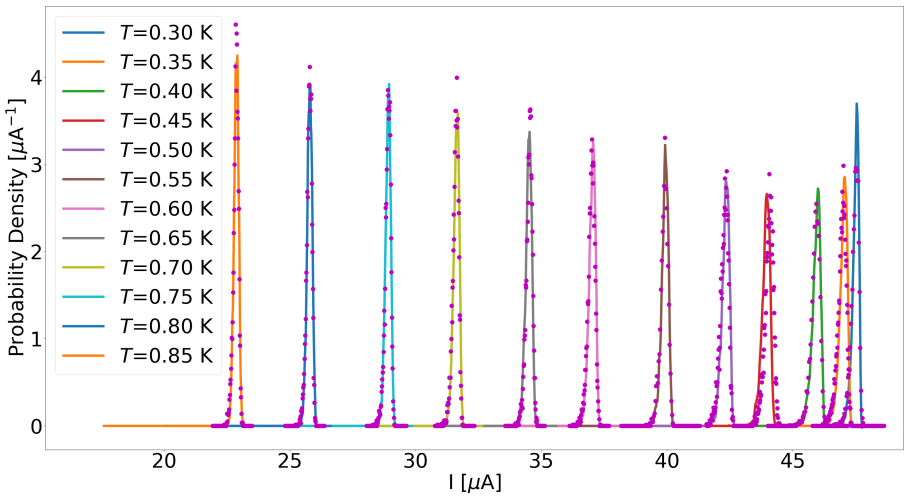

Figure 4.13: Switching current distributions at different temperatures for an Al nanowire. Solid lines are the fitting curves obtained by simulations, whereas the points are the experimental measurements.

In the increasing σ region (see Figure 4.7), i.e. $0.3 \leq T \leq 0.45$, a single phase slip model contains all physical ingredients to describe the observed $P(I)$. As the standard deviation σ decreases, the mean number of phase slips (NPS) increases as anticipated in Section 2.4. The behaviour of the mean NPS as a function of the temperature T is shown in Figure 4.14. These results are consistent with results in Ref. [29].

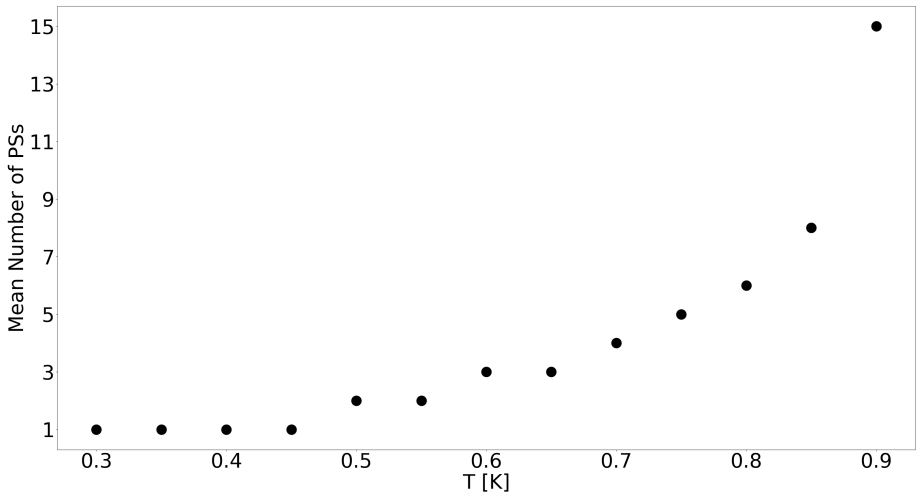

Figure 4.14: Mean number of phase slips as a function of the bath temperature T for Al nanowire.

Once the simulations of the Al nanowires SCDs have produced parameters in good agreement with the experimental data and conditions, the same analysis has been done on the two nanomeanders. In Figures 4.15a and 4.15b, the fitting curves of SCDs are shown and compared with the experimental measurements of NbTiN and NbN nanomeander, respectively.

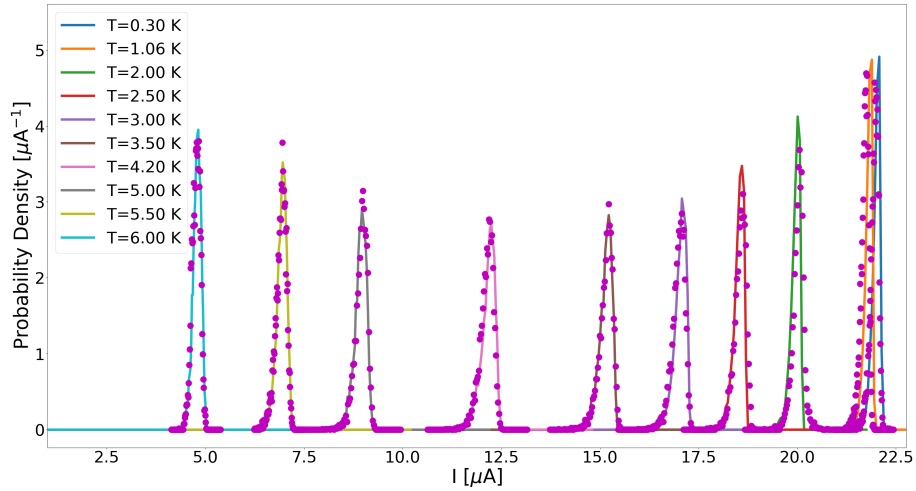

(a)

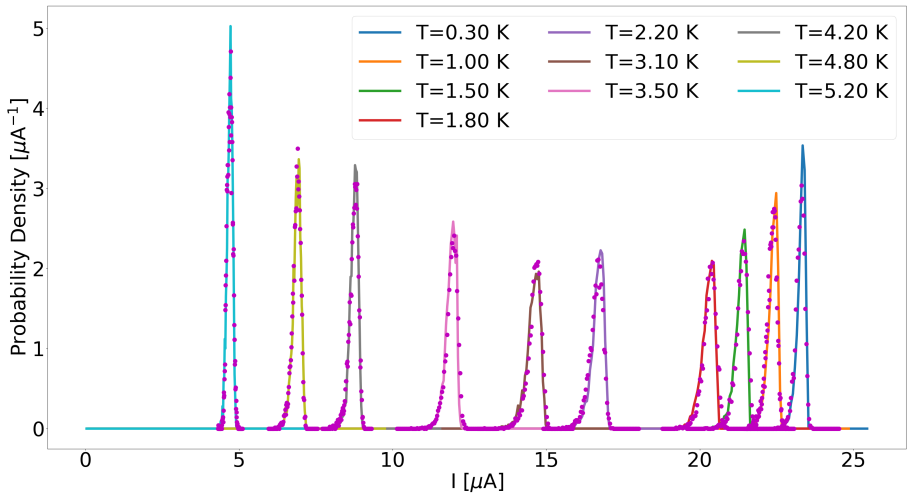

(b)

Figure 4.15: (a) Switching current distributions at different temperatures for a NbTiN nanomeander. (b) Switching current distributions at different temperatures for a NbN nanomeander. For both figures, solid lines are the fitting curves obtained by simulations, whereas the points are the experimental measurements.

As for the Al sample, for both nanomeanders, multiple phase slips are required to fit the experimental SCDs. The mean number of phase slips behaviours as a

function of the temperature T is very similar between the two nanomeander, as it can be seen in Figure 4.16a. Keeping in mind Figure 4.14, consistency can be found between the nanomeanders and the Al samples.

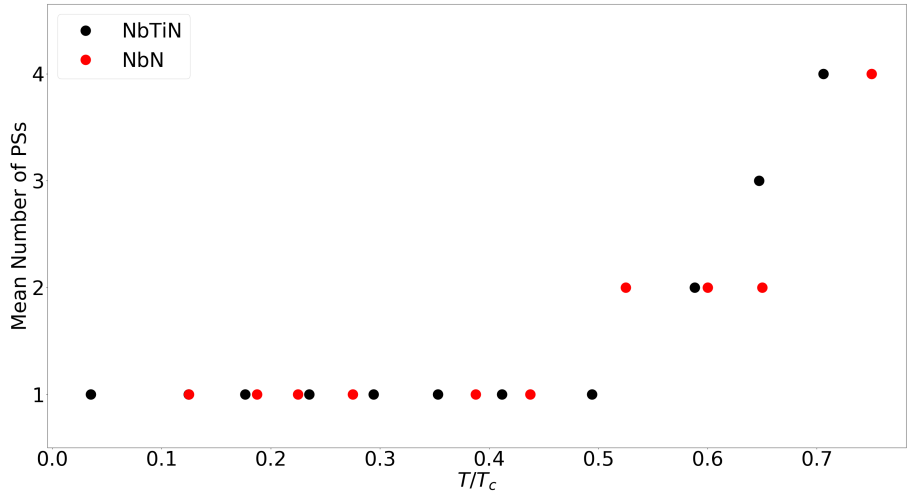

(a)

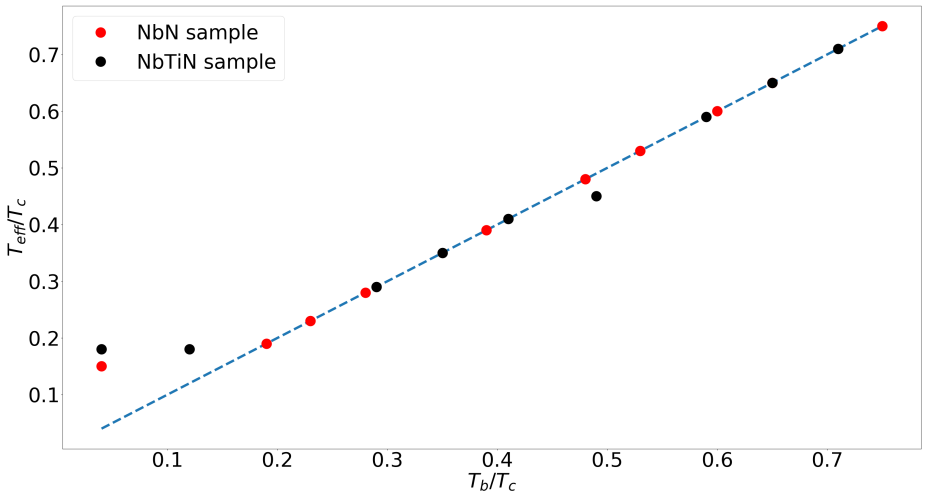

(b)

Figure 4.16: (a) Mean number of phase slips as a function of normalised temperature T/T_c for both nanomeanders. (b) Effective temperature T_{eff} normalised to the critical temperature behaviour as a function of the bath temperature T_b normalised to T_c. The blue dashed line represents the case $T_{eff} = T_b$.

Differently from Al sample, for both nanomeanders it has been necessary to use a $T_{eff} > T_b$ at low temperatures. As it is shown in Figure 4.16b, simulation curves

which satisfy the condition $T_{eff} = T_b$ are able to fit the experimental points until $T_b \sim 1\,\mathrm{K}$ ($T_b \sim 2\,\mathrm{K}$ for the NbTiN nanomeander). Physically, values of T_{eff} higher than T_b indicate that the system is not at the equilibrium with bath temperature and non-equilibrium phenomena, which are not considered in the model, are involved in the process. Indeed, at very low temperatures, the thermal conductivity reaches very low values, thus the system is not able to dissipate the energy released by the phase slip event. To better characterise tthe behavior of the standard deviation σ at very low temperatures of the two nanomeanders, other measurements of SCD have been collected between 0.01 K and 1.20 K. Experimental data and fit for the NbTiN sample are shown in Figure 4.17.

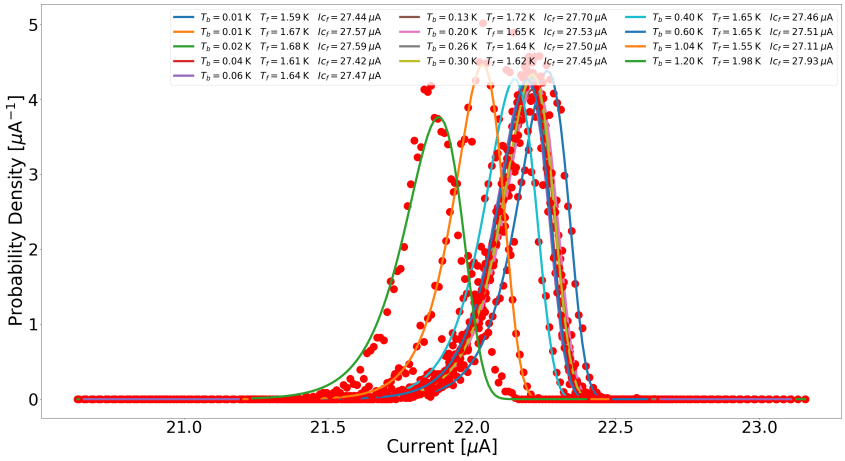

Figure 4.17: SCDs at very low temperatures. Solid lines are the best fit curves, whereas the points are the experimental data.

At extremely low temperatures, the distributions width has no significant variation below $T_b = 1\,\mathrm{K}$. Indeed, the distributions in Figure 4.17 have almost the same height and thus the same σ. For this reason, it can be stated that the distribution widths saturate around a certain σ value, which is higher than the values measured in the multiple phase slip regime. Keeping in mind the application of this sample as SNSPD, it is important to notice that lower number of dark counts correspond to small σ values. The most convenient working condition is to have a SNSPD in the multiple phase slip regime, where σ values are lower. The best condition would require the lower values of σ at about at $T = 4.2\,\mathrm{K}$, which is the reference temperature for the superconducting electronics.
In conclusion, the local heat dynamics model can be used to describe the behaviour of different nanostructures from ultracold temperatures to T_c. The samples fall in

different superconducting regimes, according to Ref. [27]. The Al sample is a standard one-dimensional system, whereas the NbN and NbTiN nanomeanders have a width $W > 10\,\xi(0)$ and for this reason are not strictly 1D nanostructures (see Sections 1.5 and 3.1). Nevertheless, the temperature behavior of critical current fluctuatons, which represents the key fingerprint to study the dissipation mechanisms in superconducting devices, can be self-consistently described by using Monte Carlo simulations based on the local heating dynamics of the system. The recognition of single and mulptiple phase slips regimes, along with the presence of non-equilibirum phenomena at very low temperatures, can be helpful in designing devices and detectors with better performances.

Conclusions

In this work, the dissipation in different superconducting nanostructures through the analysis of the switching current distributions has been studied. Al nanowires and nanomeanders made of NbTiN and NbN have been studied, due to their use as superconducting nanowire single photon detectors (SNSPD). The Al nanowires have been considered as a test sample, since their geometrical dimensions are such as to be considered a "standard" 1D superconducting nanostructures. The nanomeanders present unique features due to their impressive length (800 μm) and a width that largely exceeds the coherence length.
The self-consistency of the fitting parameters demonstrates the possibility to analyse these nanostructures in the same way, using the local heat dynamics model. Modelling allows to estimate even the number of heating events required at the different temperatures to drive the system from the superconducting to the resistive state. The number of phase slips has been correlated with the two main regions in which is possible to divide the σ behaviours as a function of T: the increasing and the decreasing σ regime. In Figure 4.18, the empty circles represents the decreasing regime points, whereas the filled circles are the increasing regime points. In the increasing distribution width region, a single phase slip is enough nduce the superconducting to the resistive transition. Instead, multiple phase slips are necessary to make a transition to happen in the decreasing regime.

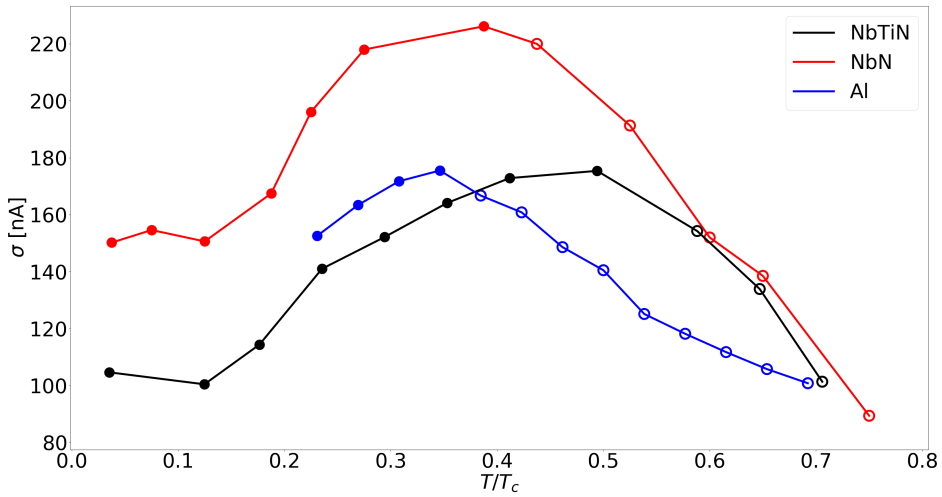

Figure 4.18: σ behaviours as a function of the temperature T for each sample. The filled circles are the σ values in the single phase slip regime, whereas the empty circles are the σ values in the multiple phase slip regime.

Concerning the two nanomeanders, the single phase slip regime shows a saturation regime at very low temepratures, which has been explained as a consequence of non-equilibrium phenomena. Indeed, at low temperatures, the thermal conductivity reachs very low values and the heat produced in the phase slip process is not able to be rapidly dissipated and increases the effective temperature of the sample.
Moreover, the σ values at low temperatures are higher than the values reached in the multiple phase slip regime, thus indicating that superconducting nanowires detectors would work better at higher temperatures, where dark counts are expected to be lower.
The future perspectives are to improve the model in order to consider out-of-equilibrium process at very low temperatures, for a better characterisation of the saturation regime. This will be relevant for possible applications in the fields of quantum communications and computing, where a full comprehension of the dynamics at ultracold temperatures is needed.

Bibliography

[1] G. Webb, F. Marsiglio, and J. Hirsch, "Superconductivity in the elements, alloys and simple compounds," *Physica C: Superconductivity and its applications*, vol. 514, pp. 17–27, 2015.

[2] H. Kamerlingh Onnes, "The resistance of pure mercury at helium temperatures," *Commun. Phys. Lab. Univ. Leiden, b*, vol. 120, 1911.

[3] W. Meissner and R. Ochsenfeld, "Ein neuer effekt bei eintritt der supraleitfähigkeit," *Naturwissenschaften*, vol. 21, no. 44, pp. 787–788, 1933.

[4] F. London and H. London, "The electromagnetic equations of the supraconductor," *Proceedings of the Royal Society of London. Series A-Mathematical and Physical Sciences*, vol. 149, no. 866, pp. 71–88, 1935.

[5] L. P. Gor'kov, "Microscopic derivation of the Ginzburg-Landau equations in the theory of superconductivity," *Sov. Phys. JETP*, vol. 9, no. 6, pp. 1364–1367, 1959.

[6] W. A. Little, "Decay of persistent currents in small superconductors," *Physical Review*, vol. 156, no. 2, p. 396, 1967.

[7] V. Z. Kresin and S. A. Wolf, *Fundamentals of superconductivity*. Springer Science & Business Media, 2013.

[8] F. London, *Superfluids: Macroscopic theory of superconductivity*, vol. 1. John Wiley & Sons, 1950.

[9] W. Corak, B. Goodman, C. Satterthwaite, and A. Wexler, "Exponential temperature dependence of the electronic specific heat of superconducting vanadium," *Physical Review*, vol. 96, no. 5, p. 1442, 1954.

[10] M. Tinkham, *Introduction to superconductivity*. Courier Corporation, 2004.

[11] F. Altomare and A. M. Chang, *One-dimensional superconductivity in nanowires*. John Wiley & Sons, 2013.

[12] A. Barone and G. Paterno, *Physics and applications of the Josephson effect*. Wiley, 1982.

[13] J. Bardeen, L. N. Cooper, and J. R. Schrieffer, "Theory of superconductivity," *Physical Review*, vol. 108, no. 5, p. 1175, 1957.

[14] V. Ginzburg and L. Landau, "Phenomenological theory," *J. Exp. Theor. Phys. USSR*, vol. 20, p. 1064, 1950.

[15] D. L. Landau and E. M. Lifsits, *Fisica statistica: parte seconda: teoria dello stato condensato*.
Editori riuniti, 1981.

[16] J. S. Langer and V. Ambegaokar, "Intrinsic resistive transition in narrow superconducting channels," *Physical Review*, vol. 164, no. 2, p. 498, 1967.

[17] U. of Cambridge, "Type i vs type ii,https://www.doitpoms.ac.uk/tlplib/superconductivity

[18] A. A. Abrikosov, "On the magnetic properties of superconductors of the second group," *Sov. Phys. JETP*, vol. 5, pp. 1174–1182, 1957.

[19] A. Schmid, "A time dependent Ginzburg-Landau equation and its application to the problem of resistivity in the mixed state," *Physik der kondensierten Materie*, vol. 5, no. 4, pp. 302–317, 1966.

[20] L. Gor'Kov, "Theory of superconducting alloys in a strong magnetic field near the critical temperature," *Soviet Physics JETP*, vol. 10, p. 998, 1960.

[21] B. D. Josephson, "Possible new effects in superconductive tunnelling," *Physics Letters*, vol. 1, no. 7, pp. 251–253, 1962.

[22] P. W. Anderson and J. M. Rowell, "Probable observation of the Josephson superconducting tunneling effect," *Physical Review Letters*, vol. 10, no. 6, p. 230, 1963.

[23] D. Massarotti and F. Tafuri, *Phase Dynamics and Macroscopic Quantum Tunneling*, pp. 455–512.
Cham: Springer International Publishing, 2019.

[24] N. Marrocco, G. P. Pepe, A. Capretti, L. Parlato, V. Pagliarulo, G. Peluso, A. Barone, R. Cristiano, M. Ejrnaes, A. Casaburi, N. Kashiwazaki, T. Taino, H. Myoren, and R. Sobolewski, "Strong critical current density enhancement in NiCu/NbN superconducting nanostripes for optical detection," *Applied Physics Letters*, vol. 97, no. 9, p. 092504, 2010.

[25] A. Murphy, A. Semenov, A. Korneev, Y. Korneeva, G. Gol'tsman, and A. Bezryadin, "Three temperature regimes in superconducting photon detectors: quantum, thermal and multiple phase-slips as generators of dark counts," *Scientific reports*, vol. 5, no. 1, pp. 1–10, 2015.

[26] X. Yang, L. You, L. Zhang, C. Lv, H. Li, X. Liu, H. Zhou, and Z. Wang, "Comparison of superconducting nanowire single-photon detectors made of NbTiN and NbN thin films," *IEEE Transactions on Applied Superconductivity*, vol. 28, no. 1, pp. 1–6, 2017.

[27] K. Likharev, "Superconducting weak links," *Reviews of Modern Physics*, vol. 51, no. 1, p. 101, 1979.

[28] A. Bezryadin, *Superconductivity in nanowires*.
Wiley Online Library, 2013.

[29] X. D. Baumans, V. S. Zharinov, E. Raymenants, S. B. Alvarez, J. E. Scheerder, J. Brisbois, D. Massarotti, R. Caruso, F. Tafuri, E. Janssens, *et al.*, "Statistics of localized phase slips in tunable width planar point contacts," *Scientific reports*, vol. 7, p. 44569, 2017.

[30] P. Li, P. M. Wu, Y. Bomze, I. V. Borzenets, G. Finkelstein, and A. Chang, "Switching currents limited by single phase slips in one-dimensional superconducting al nanowires," *Physical Review Letters*, vol. 107, no. 13, p. 137004, 2011.

[31] F. Altomare, A. M. Chang, M. R. Melloch, Y. Hong, and C. W. Tu, "Evidence for macroscopic quantum tunneling of phase slips in long one-dimensional superconducting Al wires," *Physical review letters*, vol. 97, no. 1, p. 017001, 2006.

[32] M. Ejrnaes, D. Salvoni, L. Parlato, D. Massarotti, R. Caruso, F. Tafuri, X. Yang, L. You, Z. Wang, G. Pepe, *et al.*, "Superconductor to resistive state switching by multiple fluctuation events in NbTiN nanostrips," *Scientific reports*, vol. 9, no. 1, p. 8053, 2019.

[33] C. Qiu and T. Qian, "Numerical study of the phase slip in two-dimensional superconducting strips," *Physical Review B*, vol. 77, no. 17, p. 174517, 2008.

[34] M. Bell, A. Sergeev, V. Mitin, J. Bird, A. Verevkin, and G. Gol'tsman, "One-dimensional resistive states in quasi-two-dimensional superconductors: Experiment and theory," *Physical Review B*, vol. 76, no. 9, p. 094521, 2007.

[35] W. A. Little, "Decay of persistent currents in small superconductors," *Physical Review*, vol. 156, no. 2, p. 396, 1967.

[36] D. McCumber and B. Halperin, "Time scale of intrinsic resistive fluctuations in thin superconducting wires," *Physical Review B*, vol. 1, no. 3, p. 1054, 1970.

[37] D. Pekker, N. Shah, M. Sahu, A. Bezryadin, and P. M. Goldbart, "Stochastic dynamics of phase-slip trains and superconductive-resistive switching in current-biased nanowires," *Phys. Rev. B*, vol. 80, p. 214525, Dec 2009.

[38] M. Tinkham and C. Lau, "Quantum limit to phase coherence in thin superconducting wires," *Applied Physics Letters*, vol. 80, no. 16, pp. 2946–2948, 2002.

[39] N. Shah, D. Pekker, and P. M. Goldbart, "Inherent stochasticity of superconductor-resistor switching behavior in nanowires," *Phys. Rev. Lett.*, vol. 101, p. 207001, Nov 2008.

[40] J. Kurkijärvi, "Intrinsic fluctuations in a superconducting ring closed with a Josephson junction," *Physical Review B*, vol. 6, no. 3, p. 832, 1972.

[41] T. Fulton and L. Dunkleberger, "Lifetime of the zero-voltage state in Josephson tunnel junctions," *Physical Review B*, vol. 9, no. 11, p. 4760, 1974.

[42] D. Massarotti, D. Stornaiuolo, P. Lucignano, L. Galletti, D. Born, G. Rotoli, F. Lombardi, L. Longobardi, A. Tagliacozzo, and F. Tafuri, "Breakdown of the escape dynamics in Josephson junctions," *Physical Review B*, vol. 92, no. 5, p. 054501, 2015.

[43] R. A. Ferrell, "Specific heat of a BCS superconductor," *Annalen der Physik*, vol. 505, no. 3, pp. 267–278, 1993.

[44] R. Bardeen and Tewordt, "Theory of the thermal conductivity of superconductors," *Phys. Rev*, vol. 113, p. 982, 1959.

[45] N. Kopnin, *Theory of nonequilibrium superconductivity*, vol. 110. Oxford University Press, 2001.

[46] M. Tinkham, J. Free, C. Lau, and N. Markovic, "Hysteretic I-V curves of superconducting nanowires," *Physical Review B*, vol. 68, no. 13, p. 134515, 2003.

[47] W. Zhang, L. You, H. Li, J. Huang, C. Lv, L. Zhang, X. Liu, J. Wu, Z. Wang, and X. Xie, "NbN superconducting nanowire single photon detector with efficiency over 90% at 1550 nm wavelength operational at compact cryocooler temperature," *Science China Physics, Mechanics & Astronomy*, vol. 60, no. 12, p. 120314, 2017.

[48] I. Esmaeil Zadeh, J. W. Los, R. B. Gourgues, V. Steinmetz, G. Bulgarini, S. M. Dobrovolskiy, V. Zwiller, and S. N. Dorenbos, "Single-photon detectors combining high efficiency, high detection rates, and ultra-high timing resolution," *Appl. Photonics*, vol. 2, no. 11, p. 111301, 2017.

[49] A. Y. Mironov, D. M. Silevitch, T. Proslier, S. V. Postolova, M. V. Burdastyh, A. K. Gutakovskii, T. F. Rosenbaum, V. V. Vinokur, and T. I.

Baturina, "Charge Berezinskii-Kosterlitz-Thouless transition in superconducting NbTiN films," *Scientific reports*, vol. 8, no. 1, p. 4082, 2018.

[50] A. Semenov, B. Günther, U. Böttger, H.-W. Hübers, H. Bartolf, A. Engel, A. Schilling, K. Ilin, M. Siegel, R. Schneider, *et al.*, "Optical and transport properties of ultrathin NbN films and nanostructures," *Physical Review B*, vol. 80, no. 5, p. 054510, 2009.

[51] F. Pobell, *Matter and methods at low temperatures*, vol. 2.
Springer, 2007.

[52] L. Cryotronics, *Sensor*.

[53] J. R. Taylor, *Introduzione all'analisi degli errori: lo studio delle incertezze nelle misure fisiche*.
Zanichelli, 1986.

[54] A. Elmurodov, F. Peeters, D. Vodolazov, S. Michotte, S. Adam, F. d. M. de Horne, L. Piraux, D. Lucot, and D. Mailly, "Phase-slip phenomena in NbN superconducting nanowires with leads," *Physical Review B*, vol. 78, no. 21, p. 214519, 2008.

[55] M. Sahu, M.-H. Bae, A. Rogachev, D. Pekker, T.-C. Wei, N. Shah, P. M. Goldbart, and A. Bezryadin, "Individual topological tunnelling events of a quantum field probed through their macroscopic consequences," *Nature Physics*, vol. 5, no. 7, pp. 503–508, 2009.

[56] J. M. Martinis, M. H. Devoret, and J. Clarke, "Experimental tests for the quantum behavior of a macroscopic degree of freedom: The phase difference across a josephson junction," *Physical Review B*, vol. 35, no. 10, p. 4682, 1987.